scientific data

Check for updates

OPEN

DATA DESCRIPTOR

A high resolution, gridded product for vapor pressure deficit using Daymet

Nicholas K. Corak[1,2], Peter E. Thornton[3] & Lauren E. L. Lowman[1,2] ✉

Vapor pressure deficit (VPD) is a critical variable in assessing drought conditions and evaluating plant water stress. Gridded products of global and regional VPD are not freely available from satellite remote sensing, model reanalysis, or ground observation datasets. We present two versions of the first gridded VPD product for the Continental US and parts of Northern Mexico and Southern Canada (CONUS+) at a 1 km spatial resolution and daily time step. We derived VPD from Daymet maximum daily temperature and average daily vapor pressure and scale the estimates based on (1) climate determined by the Köppen-Geiger classifications and (2) land cover determined by the International Geosphere-Biosphere Programme. Ground-based VPD data from 253 AmeriFlux sites representing different climate and land cover classifications were used to improve the Daymet-derived VPD estimates for every pixel in the CONUS+ grid to produce the final datasets. We evaluated the Daymet-derived VPD against independent observations and reanalysis data. The CONUS+ VPD datasets will aid in investigating disturbances including drought and wildfire, and informing land management strategies.

Background & Summary

Continental scale droughts are expected to become more frequent as climate change induced increases in surface temperatures lead to atmospheric drying[1]. Higher surface temperatures and less frequent precipitation during drought drive competition for water between the land surface and the atmosphere[2]. Reduced precipitation and increased atmospheric demand for water lead to soil moisture anomalies, limiting water available for plant use[3]. During droughts, water stress can reduce vegetation growth[4] and productivity[5], minimizing the role of vegetation as a carbon sink[6] and diminishing crop yields[7]. High atmospheric aridity, measured as vapor pressure deficit (VPD), has been shown to be as important as low soil moisture at driving plant water stress[8]. High VPD has also been associated with drying out vegetation, which then serves as potential fuel for wildfires[9]. With drought conditions expected to worsen through the 21st century, further attention should be paid to expanding the study of complex biological and ecohydrological responses to increased atmospheric aridity[10]. To do so, high spatial and temporal resolution datasets of VPD must be available for the scientific community. Here we present the first daily gridded VPD product for the continental United States, including parts of Northern Mexico and Southern Canada (CONUS+).

VPD has been identified as a major factor in driving water fluxes between the land surface and the atmosphere[6,11,12], impacting photosynthesis[6] and plant growth[4]. Vegetation growth responds differently to rising VPD depending on plant type and climate[13,14]. Thus, there is a need to better understand how plants modulate or adapt to changes in atmospheric aridity across gradients of climates and vegetation types. Some plants close their pores, known as stomata, during periods of elevated VPD in order to conserve water and prevent desiccation[15] and hydraulic failure[16]. Under hydraulic failure, plants can no longer exchange water and carbon with the atmosphere, leading to reduced carbon uptake and increased likelihood of plant mortality[14,17]. Elevated values of atmospheric aridity have been shown to decrease plant growth[4] and shutdown stomatal conductance and photosynthesis rates[18], indicating carbon assimilation is highly sensitive to changes in VPD.

Elevated VPD is associated with decreases in crop yields[10] which can cause billions of dollars in financial losses for the agricultural sector[7]. In arid regions of Northern China, reductions in wheat, maize, and soybean yields were shown to be more sensitive to changes in VPD than precipitation or temperature[19]. Similar

[1]Department of Engineering, Wake Forest University, Winston-Salem, NC, USA. [2]Department of Physics, Wake Forest University, Winston-Salem, NC, USA. [3]Environmental Sciences Division and Climate Change Science Institute, Oak Ridge National Laboratory, Oak Ridge, TN, USA. ✉e-mail: lowmanle@wfu.edu

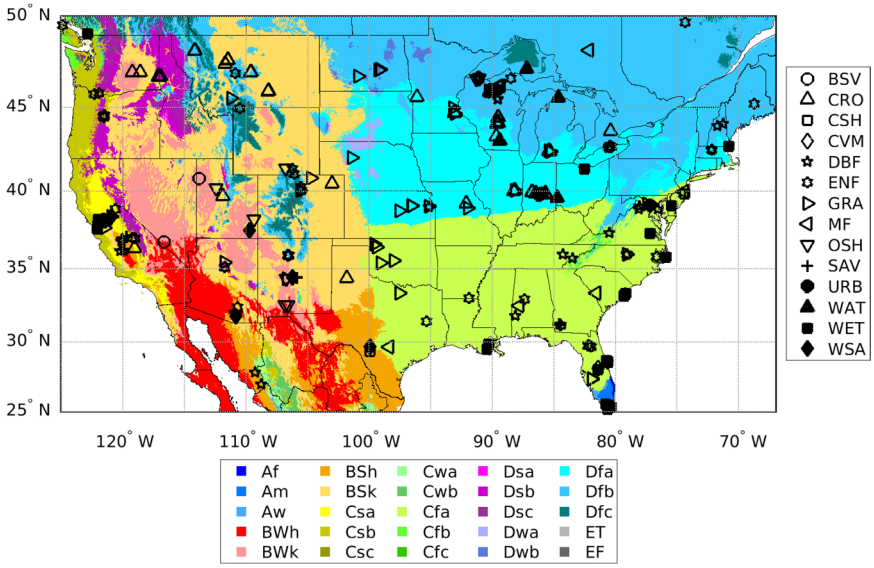

Fig. 1 Map of Köppen-Geiger climate classification on the 1 km by 1 km CONUS+ grid. The color scheme was adopted from Peel *et al.*[67]. The 253 AmeriFlux sites are indicated with markers representing the IGBP Vegetation Land Cover.

sensitivities to rising VPD have been shown in crops yields in the Midwestern US[5], central Europe[20], and northeast Australia[21]. Lobell *et al.*[5] found that maize and soybean yields in Iowa, Illinois, and Indiana have become increasingly sensitive to high VPD, though farmers are combating yield loss with agronomic advances. In Hungary, positive VPD anomalies, which are associated with increasing temperatures, were shown to negatively impact crop yield for winter wheat[20]. As climate trends point to higher surface temperatures, the detrimental effects of VPD on crop yields are expected to increase[22]. On the other hand, there is evidence to suggest high VPD may indeed have a positive effect on certain crop yields in fields with sufficient soil moisture due to plant adaptations that increase water-use efficiency[23]. Moreover, under simulated climate change conditions with projected increases in temperature and carbon dioxide, elevated carbon dioxide levels may offset the detrimental impacts of high VPD on sorghum grain yield by increasing radiation and transpiration efficiency[21]. Given the uncertainty in crop responses to rising VPD[9] in a changing climate, further analyses incorporating daily-scale VPD are needed[10].

High VPD has also been associated with the drying of surface fuels[24], increasing the risk of wildfire intensity[25] and burned area[26]. Future climate projections indicate much of the global land area is subject to increases in temperature, resulting in changes to precipitation regimes and wildfire risk[27]. Increases in VPD as a result of the feedback between rising temperature and lack of precipitation are linked to increases in recent wildfire activity in the western US[28,29]. Even in humid regions like the Pacific Northwest or Southeast, variability in precipitation resulting from climate change increases the likelihood of drought-induced wildfires[30,31]. Furthermore, high VPD increases wildfire risk in forest biomes around the globe and jeopardizes their roles as carbon sinks[32].

According to the Clausius-Clapeyron relationship[33], the amount of water the atmosphere can hold is temperature dependent. As temperatures increase, the capacity for the atmosphere to hold water increases as well[34]. VPD represents the difference between the actual amount of water vapor in the atmosphere and the amount of water vapor the atmosphere can hold at saturation. It is a measure of atmospheric demand for, or capacity to hold, water[35–37]. To better understand how projected increases in VPD will impact water fluxes during drought and increase the risk of fire at local, regional, and continental scales, there is a need for a high-resolution VPD dataset that considers climate and land cover across ecoregions. Currently, research and operations that require VPD for their analyses often have to compute VPD from ground-based[38,39] or satellite remote sensing[40,41] measurements of temperature and relative humidity because most datasets do not contain VPD measurements. Ecosystem-to-continental scale modeling and observational studies analysing plant responses to increased VPD would benefit from a fine scale, gridded VPD data product, like the one presented here.

Current available datasets that contain VPD for CONUS are point-scale measurements. The observational network AmeriFlux[42] provides sub-daily measurements of temperature and relative humidity from eddy covariance flux towers and, for select sites, provides VPD for users. AmeriFlux has ~500 sites spread across North and South America, with many sites concentrated near agricultural areas, specific research stations, and universities. As a result, there are large areas missing ground observations, including parts of the Rocky Mountains and the Great Basin Desert[43] (Fig. 1). Despite the sparse distribution of AmeriFlux sites across the United States, the diversity of land cover types and climate regions are well-represented[44].

At present, there is no single gridded dataset of VPD for all of CONUS that is freely available. Moreover, to our knowledge, no dataset has derived VPD while accounting for specific land cover and climate types. There are, however, existing methods to produce gridded, continental-scale VPD data from reanalysis or satellite-remote sensing. One limitation related to using these approaches is the coarse spatial or temporal

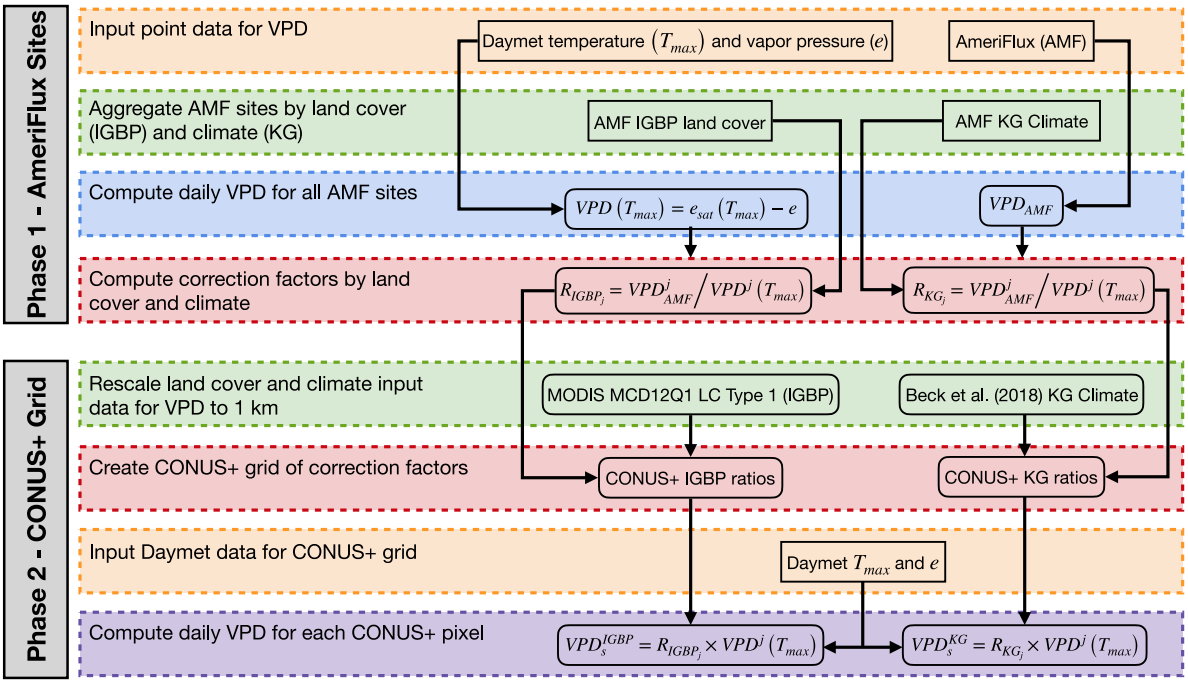

Fig. 2 Two-phase summary of workflow. In Phase 1, we use AmeriFlux VPD to correct estimates of VPD derived from Daymet variables maximum daily temperature, T_{max} and average daily vapor pressure e. In Phase 2, we apply correction factors to every grid cell in CONUS+ by matching each grid cell with the corresponding International Geosphere-Biosphere Programme (IGBP) and the Köppen-Geiger (KG) climate classification.

resolution of freely-available datasets. The North American Land Data Assimilation system (NLDAS-2) is a reanalysis dataset that provides hourly temperature, pressure, and specific humidity at an 1/8th degree (~12.5 km) spatial resolution that can be used to derive estimates of VPD[8]. The European Centre for Medium-Range Weather Forecasts (ECMWF) also produces an hourly global reanalysis dataset of meteorological variables, ERA5[45], with a horizontal spatial resolution of 31 km, which can be used to compute VPD[46]. Though the hourly resolution of the reanalysis data is useful for when accounting for diurnal fluctuations in VPD, the large spatial resolution extends beyond the fetch of an eddy covariance tower[47]. Zhang *et al.*[40] demonstrated how to compute daily VPD over China using satellite imagery from the Moderate Imaging Spectroradiometer (MODIS) at a 1 km spatial resolution. The method, which uses MODIS to estimate temperature and humidity, derives an empirical relationship from ground observations. The method is only valid in sites with weather stations and is prone to cloud contamination of surface reflectance[40]. Moreover, the 8-day observations likely do not capture day-to-day fluctuations in land surface and atmospheric water statuses that impact VPD. To overcome the limitations of the previously mentioned approaches to estimating VPD, we integrated climate and land cover classifications with ground-based observations from AmeriFlux, along with a validated high-resolution temperature and atmospheric vapor pressure product available at a 1 km spatial resolution and daily timestep. This approach informs estimates of VPD, culminating in a gridded VPD product for all of CONUS+. The CONUS+VPD datasets generated in this study have wide ranging applications: VPD can be used to study ecosystem functioning[9,14,38,48,49], drought monitoring and prediction[8,50,51], or assessing fire risk[24–26,52,53].

Methods

Overview. In this study, we used meteorological variables of average daily atmospheric vapor pressure (e) and maximum daily temperature (T_{max}) from Daymet[54], alongside ground based VPD from AmeriFlux eddy covariance towers with a variety of land cover and climate types (Fig. 1), to produce a high-resolution (1 km, daily) gridded VPD data product for CONUS+. Deriving estimates of VPD for CONUS+ consisted of two phases (Fig. 2): (1) Develop land cover and climate dependent correction factors using AmeriFlux observations, (2) Apply correction factors to all pixels in the CONUS+ grid. In Phase 1, we first computed 24-hour average VPD from 253 AmeriFlux sites with varying climate and land cover classifications. We then calculated VPD using Daymet e and T_{max}. We chose to use T_{max} instead of another daily temperature averaging scheme (e.g.[37,55–57]) because using T_{max} better recreates day-to-day variability in VPD. However, it also overestimates daily VPD (Fig. 3). In order to correct the overestimation, we computed the median ratio of AmeriFlux to Daymet-derived VPD for each land cover type and climate classification. In Phase 2, we estimated VPD for the entire CONUS+ grid. We adjusted the Daymet-derived VPD for each grid cell based on its climate or land cover type by applying the corresponding correction factor (i.e., median ratio) developed in Phase 1. This generated two 24-hour average VPD datasets: one informed by land cover and one informed by climate. The resulting Daymet-derived VPD datasets for CONUS+ are evaluated against daily average VPD computed from hourly AmeriFlux VPD data not previously used in the analysis, NLDAS-2 derived VPD, and VPD computed using a weighted temperature averaging scheme.

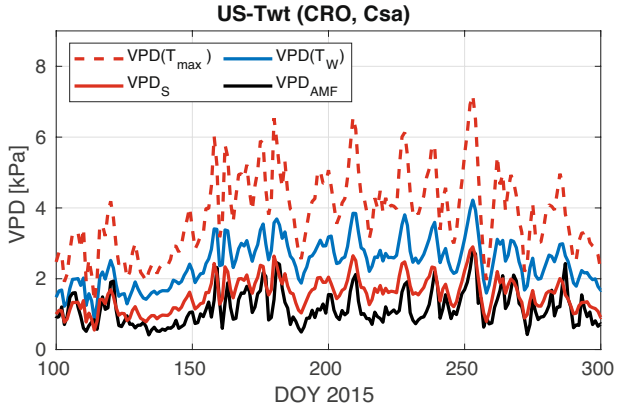

Fig. 3 Example of scaling *VPD* (T_{max}) and comparisons with AmeriFlux VPD at US-Twt for days 100–300 of 2015. US-Twt is a rice paddy cropland (CRO) AmeriFlux site in central California with a dry, temperate climate with a hot summer (Csa).

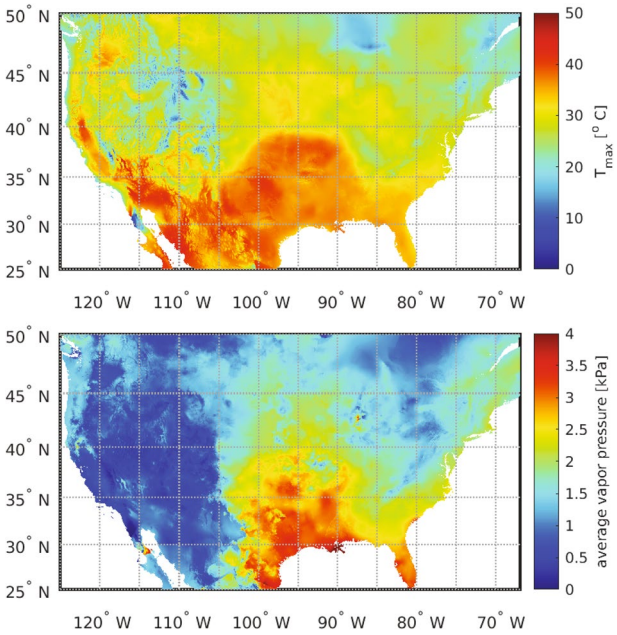

Fig. 4 Daymet maximum temperature and average vapor pressure for day 180 (i.e. June 29) 2023.

Datasets. *Daymet.* Daymet is a freely available collection of daily, 1 km, gridded meteorological data products derived from weather stations throughout North America[58]. Weather station data is used to inform daily estimates of Daymet's primary output variables: minimum and maximum temperature (T_{min} and T_{max}, respectively) and total precipitation. Daymet also produces secondary variables of average daytime shortwave radiation, average atmospheric water vapor pressure (e), and accumulated snow water equivalent, which are derived from the primary variables[59,60]. Day length is also provided as an estimate based on geographic location[58]. For this study, we used Daymet T_{min}, T_{max}, and e from 1995 to 2023, corresponding with available data records from ground based AmeriFlux eddy covariance towers. T_{min} and T_{max} were used to estimate saturated vapor pressure, e_{sat}, from which we subtract e to estimate VPD.

For this study, daily minimum and maximum temperature and average vapor pressure were acquired from the Daymet Version V4R1[54] (Fig. 4). Daymet data were directly downloaded from https://daac.ornl.gov/. Daymet V4R1 updated V4 by correcting a daily data feed error and imputing missing readings for 2020 and 2021[58]. Daymet V4 uses weather inputs from the National Centers for Environment Information Global Historical Climate Network Daily database. Daymet V4 updated previous Daymet algorithms to account for observation reporting time and high elevation biases which can affect daily maximum temperature and precipitation accumulations. For each 1 km by 1 km Daymet grid cell, a normalized weighted interpolation is used to estimate both T_{min} and T_{max} from three-dimensional temperature gradients using data from weather stations within a predefined search radius[58]. Daily average vapor pressure, e is computed using T_{min} as a proxy for dew point temperature and implementing aridity adjustments[61] which require potential evapotranspiration derived from shortwave radiation[60].

IGBP code	IGBP number	description	site years
ENF	1	Evergreen Needleleaf Forests	413.8
DBF	4	Deciduous Broadleaf Forests	146.6
MF	5	Mixed Forests	52.3
CSH	6	Closed Shrublands	16.6
OSH	7	Open Shrublands	58.1
WSA	8	Woody Savannas	51.4
SAV	9	Savannas	51.8
GRA	10	Grasslands	235.7
WET	11	Permanent Wetlands	127.8
CRO	12	Croplands	208.3
URB	13	Urban and Built-up	8.4
CVM	14	Cropland/Natural Vegetation Mosaics	5.6
BSV	16	Barren/Sparse Vegetation	6.5
WAT	17	Water Bodies	29.8

Table 1. International Geosphere-Biosphere Programme (IGBP) land cover classifications for the 253 AmeriFlux sites used in the correction factor analysis. The corresponding number codes are from MODIS MCD12Q1 LC Type 1[63]. Site years for each classification are included and represent how many years of AmeriFlux data were available for a given land cover classification across all sites.

KG code	KG number	description	site years
BWh	4	arid, desert, hot	9.6
BWk	5	arid, desert, cold	12.1
BSh	6	arid, steppe, hot	10.9
BSk	7	arid, steppe, cold	110.6
Csa	8	temperate, dry summer, hot summer	158.9
Csb	9	temperate, dry summer, warm summer	53.5
Cwa	11	temperate, dry winter, hot summer	15.8
Cfa	14	temperate, no dry season, hot summer	328.3
Cfb	15	temperate, no dry season, warm summer	11.6
Dsa	17	cold, dry summer, hot summer	6.8
Dsb	18	cold, dry summer, warm summer	36.7
Dwb	22	cold, dry winter, warm summer	20.2
Dfa	25	cold, no dry season, hot summer	182.9
Dfb	26	cold, no dry season, warm summer	330.8
Dfc	27	cold, no dry season, cold summer	81.4
ET	29	polar, tundra	20.5

Table 2. Köppen-Geiger climate classification descriptions for 247 of the 253 AmeriFlux towers used in the correction factor analysis. Note that six sites had no climate classification listed. The corresponding number codes are from Peel *et al.*[67]. Site years for each classification are included and represent how many years of AmeriFlux data were available for a given climate classification across all sites.

AmeriFlux. AmeriFlux is a network of eddy covariance flux towers, distributed across North, Central, and South America, collecting semi-continuous measurements of carbon, water, and energy fluxes[42,44,62]. The AmeriFlux data was used for rescaling Daymet-derived VPD at the tower sites and validating the CONUS+ gridded VPD product. We downloaded all AmeriFlux data used in this study from https://ameriflux.lbl.gov/, using the "Site Search" tool to select 253 sites from the nearly 500 AmeriFlux sites by considering sites in CONUS+ which had half-hourly VPD, record lengths of at least one year, and which share their data under the AmeriFlux CC-BY-4.0 License. Time series of VPD observations are provided at half-hourly increments, with records spanning 1995 to 2023; however, most sites do not have records spanning the entire time interval. The 253 sites used in this study met the criteria of having at least one complete year of VPD observations, totaling over 1400 site years of data across all sites (Tables 1 and 2). We computed daily estimates of AmeriFlux VPD (VPD_{AMF}) by averaging over all 48 half-hour measurements within a single day. AmeriFlux reports VPD in hectopascals (hPa), except for some older sites which reported VPD in kilopascals (kPa). All VPD data from AmeriFlux were converted to units of kPa. AmeriFlux provides ancillary information about the geographic location (latitude and longitude coordinates), land cover (International Geosphere-Biosphere Programme, IBGP), and climate (Köppen-Geiger, KG) for each site. We used the IGBP and KG classifications as provided from AmeriFlux to develop relationships between AmeriFlux and Daymet daily average VPD. From the 253 sites, there were 14 unique IGBP land cover and 16 unique KG climate classifications (Tables 1 and 2, respectively). To

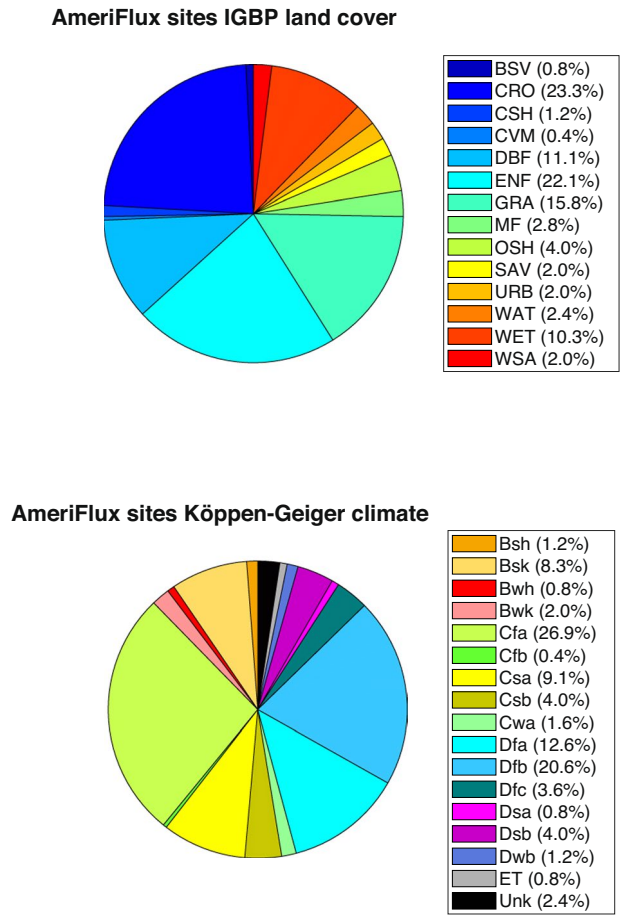

Fig. 5 Percentage breakdown of IGBP land cover and Köppen-Geiger climate classifications from the 253 AmeriFlux sites. Unk = unknown or not provided in AmeriFlux documentation.

provide independent validation, we computed daily average VPD from five AmeriFlux sites that provided hourly VPD and were not included in estimating the correction factors from Phase 1 for the final gridded CONUS+ VPD product.

A summary of the 253 AmeriFlux IGBP and KG classifications, the proportions of sites they represent, and the respective total number of site years can be found in Tables 1 and 2 and Fig. 5. KG classification Cfa (temperate, no dry season, hot summer) was the most represented classification in this analysis with 68 sites (26.9%) throughout the Southeastern US (Fig. 5). The next most common KG climate classifications was Dfb (cold, no dry season, warm summer) with 52 sites (20.6%), followed by Dfa (cold, no dry season, hot summer) with 32 sites (12.6%). Of the 253 sites in this study, croplands (CRO), evergreen needle leaf forests (ENF), and grasslands (GRA) were the most-represented IGBP land cover classifications, representing 23.3%, 22.1%, and 15.8% of the total sites, respectively. The proportion of sites a classification represents does not necessarily translate to the amount of data used in this study because some sites may have longer temporal records of VPD. For example, there are 16 more sites with KG classifications Cfa than with Dfb, but Dfb had 331 site years of data compared to Cfa which had 328 sites years of data. With 413.8 site years, ENF was the land cover classification with the most data, nearly twice as many site years as CRO despite having only three fewer tower sites. Overall, climate and land cover from AmeriFlux towers represented well the actual coverage of CONUS+ with a few exceptions. With 9.1% of sites and 158.9 site years of data, the KG classification Csa (temperate with dry, hot summer), a Mediterranean climate found in California, were over represented by the site data since only approximately 1% of the CONUS+ grid is classified as Csa. Alternatively, woody savannas (WSA) were underrepresented as they make up 2% of AmeriFlux sites but 12.6% of the CONUS+ gird.

IBGP land cover. IGBP land cover was used to classify AmeriFlux sites and for estimating VPD at the continental scale. Land cover classifications for pixels in the CONUS+ grid were generated from the Moderate Resolution Imaging Spectroradiometer (MODIS) Land Cover Type Product (MCD12Q1) Land Cover Type 1, which provides annual land cover from 2001–2023 at a 500 m spatial resolution using IGBP classes[63]. MODIS MCD12Q1 Land Cover Type 1, the Annual IGBP classification, was selected to align with the AmeriFlux provided IGBP land cover. The freely available MODIS land cover data were downloaded from A$\rho\rho$EEARS[64] (https://appeears.earthdatacloud.nasa.gov) using the "Extract Area Sample" download tool with geographic coordinate projection. The 500 m MODIS was upscaled to the Daymet 1 km grid using a nearest neighbor

Unrepresnted KG climate code		Represented KG	Climate Difference
Af, Am, Aw	→	Cfa	tropical vs temperate, no dry season, hot summer
Csc	→	Csb	cold vs warm summer
Cwb	→	Cwa	warm vs hot summer
Cfc	→	Cfb	cold vs warm summer
Dsc	→	Dsb	cold vs warm summer
Dwa	→	Dwb	hot vs warm summer
EF	→	ET	frost vs tundra

Table 3. Summary of Köppen-Geiger replacements.

interpolating algorithm. The AmeriFlux sites represented 14 of the 17 MODIS IGBP classes (Table 1). The three unrepresented IBGP land cover classes include deciduous needleleaf forests (DNF), which comprises approximately 0.005% of CONUS+ pixels, evergreen broadleaf forests (EBF) and permanent snow/ice (SNO), which together make up approximately 0.8% of pixels.

Köppen geiger climate. The gridded updated Köppen Geiger (KG) climate classifications were obtained from Beck *et al.*[65,66]. The KG classifications were also used to classify AmeriFlux sites and estimate VPD for CONUS+. The KG classifications are available at 1 km by 1 km spatial resolution, which we realigned to match the 1 km CONUS+ grid using a nearest neighbor approach. There are five main categories of classification, each broken down into subcategories, yielding a total of 30 unique classifications globally[67]. For CONUS+ grid, there were only 25 unique KG values. The AmeriFlux sites represent 16 KG classifications. In order to determine correction factors for the remaining nine KG classifications, we reclassified them following Table 3.

North American Land Data Assimilation System (NLDAS). Reanalysis data from North American Land Data Assimilation System phase 2 (NLDAS-2) Forcing File A[68] was used to estimate an independent VPD product for evaluation of the CONUS+ VPD dataset. NLDAS integrates a multitude of guage-, radar-, and model-based observations using the National Centers for Environmental Prediction (NCEP) Eta Data Assimilation System (EDAS) to generate forcing data for all of CONUS at an hourly timestep and at a 0.125° by 0.125° spatial scale[69]. The freely available NLDAS-2 variables of 2-m above ground temperature temperature (TMP), 2-m specific humidity (SPFH), and surface pressure (PRES) were downloaded using the NASA GES DISC (https://disc.gsfc.nasa.gov/) dataset subset tool[70]. VPD was calculated following the method described in Lowman *et al.*[8]. Daily average temperature from NLDAS-2 was used to estimate e_{sat} from Teten's equation and vapor pressure, e, was estimated using average daily specific humidity and air pressure.

Estimating VPD for CONUS+. In order to generate a daily gridded VPD dataset for CONUS+, we used the meteorological variables from Daymet, VPD from AmeriFlux, land cover classifications from MODIS, and climate classifications from KG. The temporal coverage of MODIS land cover was the limiting factor for the start and end dates of the data records produced in this study. At the time of development, the MODIS land cover record was 2001 to 2023, so this twenty-three-year period defined the date range for land cover correction. We assumed a single KG classification for each pixel of CONUS+ for the entire study period (i.e., no pixels changed climate classification).

Calculating VPD from Daymet - Phase 1. Calculating VPD for each AmeriFlux site required first identifying the Daymet 1 km by 1 km grid cell whose center was nearest the site's geographic coordinate and extracting the Daymet variables (Fig. 2). Daily average VPD, in kPa, was calculated as the difference between saturated, e_{sat}, and unsaturated, e, vapor pressure

$$VPD(T^*) = e_{sat}(T^*) - e \tag{1}$$

where e is provided by the Daymet daily average vapor pressure data and e_{sat} is calculated using Teten's equation[33,71]:

$$e_{sat}(T^*) = 0.611 \exp\left[A\left(\frac{T^*}{T^* + B}\right)\right]. \tag{2}$$

The variable T^* (°C) is a representative temperature computed using the Daymet maximum and minimum daily temperatures (T_{max} and T_{min}, respectively). The parameters A and B are empirically determined with $A = 17.27$ and $B = 237.15$ when $T \geq 0°C$, and $A = 21.87$ and $B = 265.5$ when $T < 0°C$[33,72]. It is a known issue that calculating saturation vapor pressure using the above freezing coefficients in Eq. 2 to below freezing temperatures results in large errors[72]. In our calculations we used $T^* = T_{max}$. Prior studies used a weighted average of T_{max} and T_{min}, $T^* = T_W = 0.606T_{max} + 0.394T_{min}$, which puts more emphasis on T_{max}[57,73]. The T_W method is presented in the earliest Daymet derivations of meteorological variables as a way to estimate average daily temperature[57]. In this method, T_{min} and T_{max} are used to fit a sine curved to simulate diurnal changes in temperature, with the average value of the sine curve representing the average value of daytime temperature[73].

IGBP code	median	mean	1 s.d.	MBE	MAE	RMSE	uRMSE	r_P
ENF	0.416	0.455	0.699	−0.019	0.176	0.247	0.246	0.840
DBF	0.405	0.447	1.579	−0.006	0.174	0.247	0.247	0.868
MF	0.369	0.389	0.260	−0.015	0.150	0.221	0.221	0.861
CSH	0.457	0.495	0.439	−0.027	0.196	0.277	0.276	0.847
OSH	0.529	0.519	0.146	−0.043	0.244	0.336	0.333	0.945
WSA	0.494	0.507	0.207	−0.031	0.282	0.378	0.377	0.903
SAV	0.445	0.448	0.189	−0.005	0.247	0.325	0.324	0.871
GRA	0.409	0.499	5.667	−0.027	0.200	0.301	0.300	0.889
WET	0.352	0.401	0.289	−0.015	0.221	0.310	0.310	0.759
CRO	0.404	0.453	0.351	−0.012	0.202	0.292	0.292	0.850
URB	0.535	0.575	0.383	−0.042	0.224	0.294	0.291	0.838
CVM	0.342	0.344	0.104	−0.004	0.158	0.201	0.201	0.690
BSV	0.507	0.515	0.280	−0.008	0.361	0.470	0.470	0.925
WAT	0.425	0.492	0.467	0.021	0.133	0.196	0.194	0.834

Table 4. Correction factors for each IGBP land cover classification with summaries of errors between observed VPD (VPD_{AMF}) and VPD scaled by IGBP land cover. Statistics include mean bias error (MBE), mean absolute error (MAE), root mean squared error (RMSE), unbiased RMSE (uRMSE), and the Pearson correlation coefficient. We applied the median correction factors in the generation of the VPD maps.

Unsaturated vapor pressure provided by Daymet uses T_{min} as a representative of dew point temperature[57]. We compared how estimating e_{sat} using T_{max} or T_W as T^* influences estimates of VPD computations.

Computing Correction Factors - Phase 1. We found that using T_W did not capture day-to-day variability in observed VPD from the AmeriFlux towers while preliminary analysis showed calculations of $VPD(T^* = T_{max})$ matched day-to-day fluctuations while overestimating daily AmeriFlux VPD (VPD_{AMF}) (Fig. 3). To reduce the difference between $VPD(T_{max})$ and VPD_{AMF}, we developed a method to scale $VPD(T_{max})$ using ratios based on AmeriFlux climate and land cover classification. In Phase 1, we computed daily $VPD(T_{max})$ for each AmeriFlux site from 1995 to 2023 and grouped all computations by KG and IGBP classifications. We computed ratios, R, of AmeriFlux to Daymet VPD at every time-step for all sites and all years with data within a given classification according to

$$R_j(t_i) = \frac{VPD^j_{AMF}(t_i)}{VPD^j(T_{max}(t_i))}, \tag{3}$$

where t_i is the daily timestep. We binned the ratios by IGBP (KG) and found the mean and median across all sites with the same land cover (climate) classification. Thus, a site with more years of data was weighted more when computing the correction factors across all sites. Because the mean values could be skewed by large outlier ratios, we used the median ratio as the correction factor for the j^{th} land cover type (climate classification) across all sites and time with land cover (climate) j,

$$R_j = \underset{j}{\text{median}}(R_j(t_i)). \tag{4}$$

There were five sites with climate listed as unknown (Unk), which were excluded from the correction factor development. We then computed new scaled VPD values at each time step, t_i by multiplying $VPD_{T_{max}}(t_i)$ by the appropriate land cover (climate) correction factor, R_j,

$$VPD^j_S(t_i) = R_j * VPD^j(T_{max}(t_i)). \tag{5}$$

Median ratios, along with their means and standard deviations, are provided for all land cover and climate classifications in Tables 4 and 5.

Generating CONUS+ VPD - Phase 2. To generate daily maps of VPD for all of the CONUS+ grid, we computed daily $VPD(T_{max})$ for every pixel and multiplied the daily value by the appropriate correction factor using Eq. 5. However, the AmeriFlux towers used to generate the correction factors only provide a sample of IGBP and KG classifications, and in some instances, the interpolated land cover and climate classification for pixels containing AmeriFlux towers may differ from the classifications provided by AmeriFlux. For the missing 3 IGBP classes mentioned above (DNF, EBF, and SNO), no correction factor was applied to the CONUS+ $VPD(T_{max})$. There were 25 out of 30 KG classes represented in the CONUS+ grid, with 16 unique KG values represented by the AmeriFlux sites, requiring the need to determine the correction factors for 9 different KG values. We used ratios from the most similar climate classifications as the correction factors for unrepresented KG values, as summarized in Table 3. The differences in KG classifications and their replacements are in the third letter of the

KG code	median	mean	1 s.d.	MBE	MAE	RMSE	uRMSE	r_P
BWh	0.498	0.476	0.163	−0.034	0.352	0.451	0.450	0.924
BWk	0.584	0.592	0.209	−0.014	0.265	0.362	0.362	0.930
BSh	0.439	0.428	0.156	0.013	0.357	0.494	0.493	0.848
BSk	0.495	0.495	0.171	−0.045	0.254	0.347	0.343	0.925
Csa	0.356	0.381	0.168	−0.040	0.279	0.395	0.393	0.840
Csb	0.404	0.400	0.205	−0.055	0.158	0.233	0.227	0.930
Cwa	0.429	0.465	0.433	−0.014	0.250	0.326	0.325	0.327
Cfa	0.397	0.433	0.271	−0.023	0.220	0.301	0.300	0.758
Cfb	0.273	0.281	0.199	−0.058	0.119	0.201	0.192	0.913
Dsa	0.367	0.368	0.160	−0.125	0.280	0.434	0.415	0.929
Dsb	0.520	0.571	0.264	0.030	0.156	0.220	0.218	0.951
Dwb	0.515	0.631	0.727	−0.041	0.257	0.342	0.339	0.800
Dfa	0.400	0.440	0.292	−0.167	0.151	0.223	0.222	0.847
Dfb	0.398	0.440	1.107	−0.015	0.145	0.212	0.211	0.852
Dfc	0.504	0.580	1.452	−0.023	0.125	0.177	0.175	0.883
ET	0.567	1.259	19.181	−0.024	0.116	0.161	0.160	0.842

Table 5. Correction factors for each Köppen-Geiger climate classification with summaries of errors between observed VPD (VPD_{AMF}) and VPD scaled by KG climate. Statistics include mean bias error (MBE), mean absolute error (MAE), root mean squared error (RMSE), unbiased RMSE (uRMSE), and the Pearson correlation coefficient. We applied the median correction factors in the generation of the VPD maps.

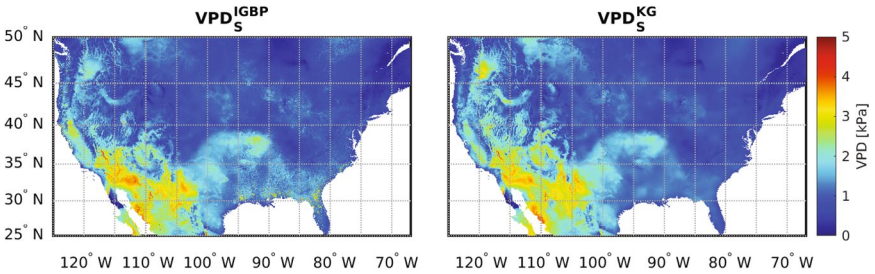

Fig. 6 Maps of the VPD_s products for June 29, 2023 (DOY 180).

short-name classifications, which indicates summer temperatures[67]. The nine unrepresented KG classes are (Af, Am, Aw, Csc, Cwb, Cfc, Dsc, Dwa, EF). KG classifications with leading "A" are all tropical, and we had no tropical climates represented in the AmeriFlux site data, however, extreme biases exist if no correction factors were applied to these pixels (i.e., $R_j = 1$), which comprise <0.3% of pixels in the humid south of Florida. So, we replaced Af, Am, and Aw, with climate Cfa which covers most of the Southeastern US, including Northern Florida.

Data Records

The dataset, along with supporting data generation and evaluation codes, are available as a resource in the HydroShare repository[74]. Two different CONUS+ VPD datasets were created: one for $VPD(T_{max})$ scaled by the Köppen-Geiger (KG) climate classification, and one scaled by MODIS Land Cover Type 1 (IGBP) classification. We provide 23 years of daily, gridded VPD data spanning the period 2001–2023. The gridded data products are available as netCDF files covering CONUS+, with bounding box 25 to 50°N latitude and 67 to 125°W longitude (Fig. 6). Each netCDF files contains one year of data, with data arrays having dimensions 5731 by 3122 by 365. The first two dimensions correspond with the dimensions of the CONUS+ grid, and the third dimension represents each day of the year. Daymet provides 365 days of temperature and vapor pressure for each day of the year. In leap years, day 365 corresponds with December 30 and no data is provided for December 31. We follow the same convention. The VPD data are stored as 16-bit unsigned integers in Pascals. Therefore, a correction factor of 10^{-3} must be applied to convert the values into units of kPa. In the repository, we also provide netCDF files of the CONUS+ grids of KG and yearly IBGP values, along with.csv files containing tables of the corresponding correction factors. NaNs (indicating not-a-number) are used to fill values where the VPD data is unavailable, which usually occurs over oceans and larger bodies of water. There are two additional scripts provided in the HydroShare repository to assist users in: (1) Plotting CONUS+ maps of VPD for any day of year and (2) Extracting VPD time series data for any location (i.e., pixel) or set of locations in the CONUS+ grid.

Method	MBE	MAE	RMSE	uRMSE	r_P
Scaled by IGBP	−0.018	0.196	0.282	0.281	0.886
Scaled by KG	−0.024	0.195	0.283	0.282	0.886
Weighted Temperature	0.184	0.275	0.419	0.377	0.849
NLDAS	0.009	0.226	0.340	0.340	0.862

Table 6. Error metrics (MBE, MAE, RMSE, uRMSE, r_P) for Daymet-derived and NLDAS VPD compared to AmeriFlux tower measurements and averaged across all sites.

Site	site years	classification	MBE	MAE	RMSE	uRMSE	$r_{Pearson}$
US-Cop	4.5	IGBP: GRA	−0.502	0.530	0.752	0.560	0.965
		KG: Bsk*	−0.334	0.396	0.566	0.456	0.965
		VPD (T_W)	−0.148	0.289	0.405	0.377	0.949
		NLDAS	−0.205	0.304	0.413	0.358	0.957
US-Cwt	5.0	IGBP: DBF	0.124	0.188	0.232	0.196	0.721
		KG:Dfb	0.114	0.182	0.225	0.194	0.721
		VPD (T_W)	0.277	0.304	0.373	0.249	0.686
		NLDAS	−0.090	0.157	0.211	0.191	0.651
US-MMS	15.1	IGBP: DBF	−0.019	0.170	0.232	0.230	0.855
		KG: Cfa	−0.029	0.171	0.232	0.231	0.855
		VPD (T_W)	0.130	0.204	0.285	0.253	0.838
		NLDAS	−0.110	0.230	0.331	0.312	0.721
US-PFa	28.9	IGBP: MF	0.014	0.114	0.164	0.163	0.865
		KG: Dfb	0.041	0.119	0.170	0.165	0.865
		VPD (T_W)	0.147	0.174	0.250	0.202	0.858
		NLDAS	−0.053	0.135	0.201	0.194	0.803
US-UMB	14.6	IGBP: DBF	−0.028	0.112	0.161	0.158	0.898
		KG: Dfb	−0.035	0.113	0.163	0.159	0.898
		VPD (T_W)	0.080	0.132	0.191	0.173	0.895
		NLDAS	−0.173	0.197	0.298	0.242	0.777

Table 7. Summary of error metrics for five independent AmeriFlux sites. AmeriFlux does not provide climate for US-Cop, but 'Bsk' is the climate from the interpolated KG climate[65].

Technical Validation

We evaluated the performance of CONUS+ scaled VPD products (VPD_S), $VPD(T_W)$, and VPD_{NLDAS} by comparing each to AmeriFlux VPD (VPD_{AMF}) using a variety of error metrics. We found that both land cover and climate informed VPD datasets compare more favorably against AmeriFlux than daily VPD estimated by average daily temperature or NLDAS-derived VPD (Table 6). We further evaluated how the method performs across specific IGBP land cover and KG climate classifications, summarized in Tables 4 and 5. Lastly, we performed independent evaluations of VPD_S at five sites that provided only hourly VPD and were not included in the correction factor development: US-Cop, US-Cwt, US-MMS, US-PFa, and US-UMB (Table 7, Fig. 7).

Error metrics. The error metrics presented are mean bias error (MBE), mean absolute error (MAE), root mean squared error (RMSE), unbiased RMSE (uRMSE), and the Pearson correlation coefficient (r_p) for each classification j at time $t_i, i \in 1, \ldots, N = 365$, and were computed as

$$MBE_j = \frac{1}{N}\sum_{i=1}^{N}(VPD_S^j(t_i) - VPD_{AMF}^j(t_i)), \tag{6}$$

$$MAE_j = \frac{1}{N}\sum_{i=1}^{N}|VPD_S^j(t_i) - VPD_{AMF}^j(t_i)|, \tag{7}$$

$$RMSE_j = \sqrt{\frac{1}{N}\sum_{i=1}^{N}(VPD_S^j(t_i) - VPD_{AMF}^j(t_i))^2}, \tag{8}$$

$$uRMSE_j = \sqrt{RMSE_j^2 - MBE_j^2}, \tag{9}$$

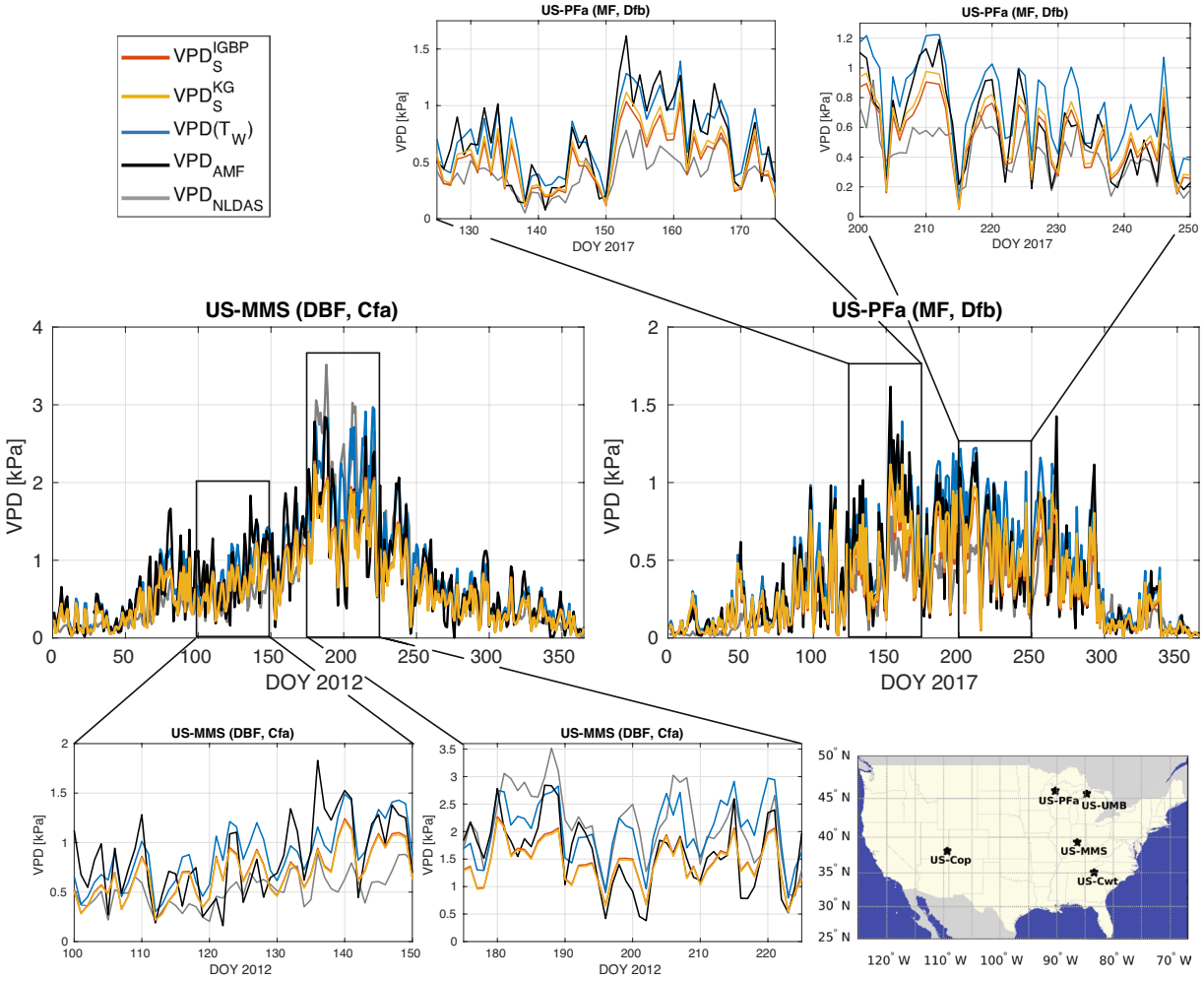

Fig. 7 Time series of scaled Daymet VPD compared with AmeriFlux, and NLDAS for US-MMS and US-PFa, and a map of the independent sites not included in the correction factor development whose error metrics are in Table 7. Pop outs show days 100–150 and 175–225 for US-MMS and days 125–175 and 200–250 for US-PFa.

and

$$r_j = \frac{\sum_{i=1}^{N}(VPD_{AMF}^{j}(t_i) - \overline{VPD}_{AMF}^{j})\sum_{i=1}^{N}(VPD_{S}^{j}(t_i) - \overline{VPD}_{S}^{j})}{\sqrt{\sum_{i=1}^{N}(VPD_{AMF}^{j}(t_i) - \overline{VPD}_{AMF}^{j})^2\sum_{i=1}^{N}(VPD_{S}^{j}(t_i) - \overline{VPD}_{S}^{j})^2}}. \quad (10)$$

The error metric MBE can be any positive or negative value while MAE and RMSE are non-negative. Positive (negative) values of MBE indicate VPD_S is greater (less) than VPD_{AMF}, on average. Here, positive MBE indicates VPD_S overestimates VPD_{AMF}. Large errors with opposite signs can negate one another in calculations of MBE, resulting in small bias errors. By taking the absolute value of each daily error, MAE provides a measure of the overall magnitude of the differences between VPD_{AMF} and VPD_S. Like MAE, squaring the difference between VPD_{AMF} and VPD_S in RMSE makes the error positive, but it also provides more weight to large error and less weight to small errors. To remove the effects of systematic bias in the bulk error estimates of RMSE for independent study sites, we computed uRMSE[75]. The Pearson correlation coefficient (r_p), which ranges between -1 and 1, is a metric of the linear relation between VPD_{AMF} and VPD_S. The closer the magnitude of r_p is to one, the more linear the relationship between the two, with the sign of r_p indicating whether or not the relationship is positive or negative. Overall, MBE, MAE, RMSE, and uRMSE closer to zero, and r_p closer to one, indicate the Daymet-derived VPD aligns well with observations from AmeriFlux.

Overall performance of correction factors. While the Pearson correlation coefficients were similar in the VPD_s, $VPD(T_W)$ and VPD_{NLDAS} methods, there were differences in the other error metrics (Table 6). The negative MBE indicates that the correction factors tended to underestimate daily averages of AmeriFlux VPD. However, for Daymet VPD scaled by IGBP or KG, those overestimates were ~0.02 kPa versus the overestimate of 0.18 kPa using a weighted temperature approximation. The MAE from scaling VPD_s was 29% smaller than $VPD(T_W)$ across all sites. The RMSE for $VPD(T_W)$ compared to VPD_{AMF} was 0.14 kPa higher than the RMSE using

the VPD_s methods. Even after removing bias, the uRMSE is stil 0.1 kPa higher than VPD_s. While VPD_{NLDAS} has better error metrics than $VPD(T_W)$, the uRMSE value of 0.340 kPa is 0.06 kPa larger than either the land cover or climate corrected VPD. The results indicate that on average, and in extreme cases, across all sites, using land cover and climate to inform the scaling of $VPD^j(T_{max})$ outperformed estimates of $VPD(T_W)$ and VPD_{NLDAS}.

Within the scaling methods, scaling VPD by land cover or by climate tended to have similar values across error metrics (Table 6), but performance varied within classifications (Tables 4 and 5). While most of the correction factors had standard deviations less than 0.4, some standard deviations were orders of magnitude larger. For example, the standard deviation for the IGBP land cover grassland (GRA) was over 5. This was due to a few large ratios (over 10) with the largest being 1067. Large ratios can happen when the denominator, in this case $VPD^j(T_{max})$, is near zero. Nearly all of the large ratios occurred in winter months with temperature below freezing. The coefficients for below freezing temperatures used in Eq. 2 to compute saturated vapor pressure allowed for saturated vapor pressure to be nearly the same as actual vapor pressure, resulting in VPD near zero (i.e. on the order of 10^{-4} kPa). In total, this happened for the IGBP land cover class GRA on 52 days, and since there were over 1400 site years of data, we did not remove these values. Data from sites US-NR3 and US-NR4 were the leading contributors to the large standard deviations for GRA, being responsible for 38 of the 52 ratios greater than 10 and all six ratios great than 100. In those instances where the ratios were greater than 100, $VPD^j(T_{max})$ (the denominator) was between 0.0002 and .0005 kPa while VPD^j_{AMF} (the numerator) fell between 0.1 and 0.2 kPa. Similarly, there was a very high standard deviation of 19.2 for the KG climate classification ET. There were only two sites that have KG classification ET, US-NR3 and US-NR4, explaining why these two classifications had higher standard deviations for the mean of the correction factors. Despite high standard deviations, the average errors associated with the application of correction factors to scale $VPD(T_{max})$ were unaffected by the few extreme values due to the total number of records used in the analysis and the fact that we adopted the median values as the correction factors when applying them to CONUS+. The magnitude of the error metrics MBE, MAE, and RMSE were smaller for the two ET sites than for the KG corrected methods across all sites (Tables 4 and 5). This suggests that the high standard deviation of the correction factors did not negatively affect the ability of the correction factors to accurately scale $VPD^j(T_{max})$.

The r_p values correlating the VPD_s and VPD_{AMF} were strong (i.e., $r_p > 0.5$) for most classifications, with most $r_p > 0.8$, the highest of which came from the open shrubland (OSH) IGBP classification, with $r_p = 0.945$ and KG climate Dsb (cold, dry, warm summer), with $r_p = 0.951$. The KG classifications Cwa (temperate, dry winter, warm summer) had the least linear relationship, $r_p = 0.327$. This classification was only represented by 4 sites (Fig. 5) and 15.6 site years (Tables 1 and 2). And while there was not as strong of a linear relationship for Cwa when compared to VPD_{AMF}, the overall accuracy indicated by other metrics validates the performance of the correction factor.

Considering, the method of scaling by IGBP land cover, the algorithm had the smallest error metrics for cropland/vegetation mosaics (CVM, Table 4) with MBE of -0.004 kPa, MAE of 0.158 kPa and RMSE of 0.201 kPa. However, there was only one site with 5.6 years of data, so CVM was not the most well represented land cover. With 56 sites and over 400 site years of data, evergreen needleleaf forests (ENF) were the most represented land cover. The correction factor median for ENF was 0.416, with a mean and standard deviation of 0.455 and 0.699, respectively. Despite the standard deviation being larger than the correction factor, there was a strong linear relationship ($r_p = 0.840$) between VPD_s and $VPD(T_{max})$. The error metrics MAE, MBE, and RMSE for ENF were comparable to the same metrics across all IGBP classifications. Climate classifications Cfb (Temperature, no dry season, warm summer) and ET (Polar tundra) had some of the lowest error metrics but were only represented by one and two sites, respectively. Classification Cfa (Temperate, no dry season, hot summer), which covers most of the Southeast US and was represented by almost 27% of the study sites with 328 site years of data, had errors only slightly worse than the average across all climates.

VPD Uncertainty Analysis. *Evaluating VPD for Independent AmeriFlux Sites.* For the correction factor development presented above, we used AmeriFlux VPD for sites that reported half-hourly data. For time series analysis, we identified five sites inside of CONUS+ that provided hourly data and were not included in the correction factor development: US-Cop (GRA, no climate reported but interpolated as Bsk), US-Cwt (DBF, Dfb), US-MMS (DBF, Cfa), US-PFa (MF, Dfb), and US-UMB (DBF, Dfb). We scaled $VPD^j(T_{max})$ for these for sites using correction factors corresponding with the AmeriFlux provided vegetation land cover and climate. Error metrics for those sites are found in Table 7 and example time series for two sites for select years are shown in Fig. 7.

Error metrics indicate strong performance of VPD_s relative to AmeriFlux VPD at US-Cwt, US-MMS, US-PFa, and US-UMB. For each of the four sites, uRMSE is smaller than the respective error for the same land cover and climate classifications (Tables 4 and 5). Performance of VPD_s is weakest at US-Cop, a grassland in a cold, arid environment. AmeriFlux tends to have higher VPD than VPD_s and VPD_{NLDAS} at this site as seen in the negative MBE values (Table 7). Error metrics for the land cover and climate corrected VPD were lower than VPD_{NLDAS} at US-MMS, US-PFa, and US-UMB, the three sites with the longest temporal records. *VPDs* and VPD_{NLDAS} differed in uRMSE at US-Cwt by 0.005 kPa, indicating that our scaled VPD generally outperforms NLDAS across the five test sites. Even for NLDAS, error metrics are highest at US-Cop. The high RMSE values of 0.752 and 0.566 for land cover and climate corrected VPD, respectively, indicate the largest errors occurred during periods of elevated VPD. The lower uRMSE values for *VPDs* indicate that our methods capture the variability in daily VPD better than alternative methods. For example, during green up at US-MMS (days 100 to 150) and the middle part of the growing season (days 175 to 225) of 2012, the land cover and climate corrected VPD compared more favorably against AmeriFlux VPD than NLDAS, which underestimated AmeriFlux during green up and overestimated AmeriFlux in days 180 to 210 of 2012 (Fig. 7), a time period of an extreme drought in the Midwest[76].

Uncertainty in Land Cover and Climate Classifications. We generated land cover and climate dependent correction factors using VPD from 253 AmeriFlux eddy covariance flux towers, however several land cover and climate classifications had less than five representative sites. For IGBP land cover, there was only one site classified as cropland/natural vegetation mosaics (CVM), two sites classified as barren sparse vegetation (BSV), and three sites classified as closed shrubland (CSH). For KG climate, one site represented classification Cfb (temperate, no dry season, warm summer), while classifications Bwh (arid, desert, hot), Dsa (cold, dry and hot summer), ET (polar tundra) each had 2 sites. Classifications Bsh (arid, steppe, hot) and Dwb (cold, dry winter, warm summer) had three sites each, and there were four sites with classification Cwa (temperate, dry winter, hot summer). No tropical sites were represented by the AmeriFlux sites. In contrast, several land cover and climate sites represented significant portions of the 253 sites. There were 59 sites classified as croplands (CRO), 56 as evergreen needleleaf forests (ENF), and 40 as grasslands (GRA). There were and 68 sites with KG climate classification Cfa (temperate, no dry season, hot summer), and 52 classified as Dfb (cold, no dry season, warm summer). It is possible that having a larger sample of underrepresented classifications, in more regions across CONUS+, could have improved performance. Additionally, most AmeriFlux sites are located in heterogeneous landscapes, and the heterogeneity has been shown to influence the variability of VPD in the local microclimate[9]. This consideration is important for researchers investigating the variability in ecosystem responses to variations in VPD.

Usage Notes

Research to Operational Applications. This dataset offers users a chance to perform fine spatial and temporal scale investigations in a variety of climate and land covers across CONUS+ which is particularly beneficial for studying areas with limited or no available ground data records of VPD. To conduct a point or other small-scale study, a user would need to identify a latitude/longitude coordinate pair (or set of coordinate pairs for multiple sites or for a small region) and the corresponding grid location(s) from the dataset. A time series of VPD could be useful for many reasons. For example, one could follow the methods described by Yuan *et al.*[4] or Li *et al.*[77] to analyze the VPD dependence of carbon assimilation on plant growth. Since the influence of VPD on vegetation growth can vary by region[19], users could separate the data by land cover or climate to explore how VPD affects carbon assimilation and plant growth vary by climate and land cover.

Because VPD is linked to drought[50], with high VPD corresponding to dry conditions, this dataset could be useful in tracking VPD anomalies that may be associated with drought identification and intensification for all of CONUS+, supporting a suite of indices and anomalies already implemented as drought markers[78]. One such index, the evaporative stress index (ESI) or ratio (ESR) considers more than precipitation anomalies by computing the ratio of actual evaporation to potential evaporation[78], which depends on VPD[79], and has been shown to effectively track rapid changes in drought conditions[80]. Generating standardized VPD anomalies in similar ways could be additionally effective ways to study the direct influence of VPD on drought development. Additionally, when analyzed with covariates such as precipitation and soil moisture[8], this dataset could be useful in identifying VPD-induced drought thresholds across land cover and climate classifications, similar to Lowman *et al.*[8].

VPD is a variable of interest to a broad range of the environmental and geophysical science communities, spanning climatology, ecology, ecophysiology, and beyond. Daymet has a meteorological record that dates back to 1980 for most of North America[58]. With over forty years of temperature and vapor pressure data, those interested in longer-term climatological studies could use this data and adapt our methods to extrapolate VPD back to 1980 and into the future to investigative how VPD is changing at climatological time scales, especially with changing land cover and climate classifications. For those interested in purely atmospheric studies, this dataset could also be useful for research investigating how vapor pressure changes within the vertical atmospheric column by providing surface or near surface VPD. Because of the wide range of altitudes spanning CONUS+, these datasets could be used with elevations maps to investigate how plant function, such as photosynthesis, varies with VPD across altitudinal gradients[81]. Fire and other disturbances, such as tropical cyclones, can impact the local VPD by altering the local climate and landscape[82]. Studies of how surface VPD anomalies impact wildfire risk[24] across land cover and climate regions in CONUS+ will benefit from using this dataset in conjunction with other fire related data products.

We anticipate land managers, using research to inform operations, to access this dataset to assess when and how crop yields begin to be impacted during VPD-induced drought, and to evaluate the resiliency of various croplands to high VPD in different climates. This type of scientific inquiry can guide agricultural strategies to mitigate the effects of changing atmospheric demand for water. Similarly, studies using these datasets to investigate the impacts of high VPD on wildfire risk could be translated into protocols for forest management decisions to determine wildfire risk status.

Alternative Ways to Use the VPD Products. We encourage users to consider the land cover and climate classifications of their study sites when using this data product. Outputs between the two VPD products are similar, but subtle differences exists (Fig. 6). In areas like the Southeastern US, where land cover can be heterogeneous but climate is homogeneous over are large region, VPD_S^{KG} tends to be smoother than VPD_S^{IGBP}. In some applications users may prefer to use daily maximum VPD (i.e., $VPD\ (T_{max})$) as a proxy for maximum daily water stress[50]. $VPD\ (T_{max})$ can be obtained for any pixel by dividing by the correction factor. Additionally, users may want to account for both climate and land cover. To do so, they would divide by the correction factor before applying a correction factor from a different classification, or some combination of correction factors. For example, if a user is working with a site and they want to combine the effects of land cover and climate classification, they could scale $VPD\ (T_{max})$ using the average of the IGBP and KG correction factors for that site. Or users could attempt to incorporate vegetation heterogeneity by combining correction factors for one or more vegetation types.

We assumed land cover changes occurred annually according to MODIS IGBP. One could update this VPD product using the newest available MODIS IGBP records in the future. Additionally, users may want to extend

records further back (prior to 2001) in which case they could assume prior land cover, with caution, and use the land cover map of correction factors to apply to earlier Daymet records. With MODIS going offline in the near future, it may also be possible to follow this procedure with different land cover classification schemes. Similarly, any updated climate classification schemes could be applied to any future Daymet data records or those prior to 2001 in order to expand the available date record of *VPD* (T_{max}). The methods presented here could also be adapted for regions across the world, especially in areas with similar climates and or land cover to CONUS+. Studies investigating VPD in arctic and tropical regions could follow the methods presented here but would benefit from a dataset developed using additional ground observations from those regions.

Transferability Outside of CONUS+. The methods presented in this manuscript can be adapted to other study regions as long as investigators account for the resolution of the temperature, vapor pressure, land cover, and climate inputs. Here, the MODIS land cover data is 500 m and the Koppen-Geiger climate 1 km, which were each resampled to align with the Daymet CONUS+ grid at 1 km. This method could be directly applied to the entire Daymet spatial coverage (Alaska, Hawaii, Puerto Rico, Mexico and Canada) because there are AmeriFlux and/or FluxNet towers to provide ground observations of VPD. Outside of those regions, Daymet is not available. Thus, some alternative meteorological data set would need to be used (e.g., Climatic Research Unit gridded Time Series[83]). The land cover and climate data are each available globally so applying the methods presented requires subsetting land cover and climate and aligning it to match the resolution of the temperature and atmospheric vapor pressure data of the new study region. FLUXNET data could be applied to a wider range of regions (e.g., South America, Africa, Asia, and Europe[42]). Otherwise, the key limitation to applying this approach is the availability of ground observations needed to build correction factors for the daily estimates of VPD.

Working with NetCDF Files. The datasets are available in netCDF file format. NetCDF files are commonly used formats for storing array data. They are easily readable by most software applications (e.g., Python, R, Matlab, Fortran, etc.). For more information and resources about netCDF files, visit https://www.unidata.ucar.edu/software/netcdf/. Additionally, users can subset, visualize, or analyze the netCDF files in the HydroShare resource using the THREDDS (Thematic Real-time Environmental Distributed Data Services) data server. For help with using THREDDS, visit https://help.hydroshare.org/apps/thredds-opendap/.

Code availability

All codes used to generate, visualize, and subset the data are freely available as part of the same resource as the VPD datasets in CUAHSI HydroShare[74].

Received: 7 October 2024; Accepted: 27 January 2025;
Published online: 12 February 2025

References

1. Dai, A., Zhao, T. & Chen, J. Climate change and drought: a precipitation and evaporation perspective. *Current Climate Change Reports* **4**, 301–312, https://doi.org/10.1007/s40641-018-0101-6 (2018).
2. Miralles, D. G., Gentine, P., Seneviratne, S. I. & Teuling, A. J. Land–atmospheric feedbacks during droughts and heatwaves: state of the science and current challenges. *Annals of the New York Academy of Sciences* **1436**, 19–35, https://doi.org/10.1111/nyas.13912 (2019).
3. Novick, K. A. *et al*. The increasing importance of atmospheric demand for ecosystem water and carbon fluxes. *Nature climate change* **6**, 1023–1027, https://doi.org/10.1038/nclimate3114 (2016).
4. Yuan, W. *et al*. Increased atmospheric vapor pressure deficit reduces global vegetation growth. *Science advances* **5**, eaax1396, https://doi.org/10.1126/sciadv.aax1396 (2019).
5. Lobell, D. B. *et al*. Greater sensitivity to drought accompanies maize yield increase in the us midwest. *Science* **344**, 516–519, https://doi.org/10.1126/science.1251423 (2014).
6. Zhao, M. & Running, S. W. Drought-induced reduction in global terrestrial net primary production from 2000 through 2009. *science* **329**, 940–943, https://doi.org/10.1126/science.1192666 (2010).
7. Otkin, J. A. *et al*. Assessing the evolution of soil moisture and vegetation conditions during the 2012 united states flash drought. *Agricultural and forest meteorology* **218**, 230–242, https://doi.org/10.1016/j.agrformet.2015.12.065 (2016).
8. Lowman, L. E., Christian, J. I. & Hunt, E. D. How land surface characteristics influence the development of flash drought through the drivers of soil moisture and vapor pressure deficit. *Journal of Hydrometeorology* **24**, https://doi.org/10.1175/JHM-D-22-0158.1 (2023).
9. Novick, K. A. *et al*. The impacts of rising vapour pressure deficit in natural and managed ecosystems. *Plant, Cell & Environment* https://doi.org/10.1111/pce.14846 (2024).
10. López, J., Way, D. A. & Sadok, W. Systemic effects of rising atmospheric vapor pressure deficit on plant physiology and productivity. *Global Change Biology* **27**, 1704–1720, https://doi.org/10.1111/gcb.15548 (2021).
11. Qin, Z. *et al*. Identification of important factors for water vapor flux and co2 exchange in a cropland. *Ecological modelling* **221**, 575–581, https://doi.org/10.1016/j.ecolmodel.2009.11.007 (2010).
12. Monteith, J. L. Evaporation and environment. In *Symposia of the society for experimental biology*, vol. 19, 205–234 (Cambridge University Press (CUP) Cambridge, 1965).
13. Liu, M. *et al*. Overridingly increasing vegetation sensitivity to vapor pressure deficit over the recent two decades in china. *Ecological Indicators* 111977, https://doi.org/10.1016/j.ecolind.2024.111977 (2024).
14. Grossiord, C. *et al*. Plant responses to rising vapor pressure deficit. *New Phytologist* **226**, 1550–1566, https://doi.org/10.1111/nph.16485 (2020).
15. Merilo, E. *et al*. Stomatal vpd response: there is more to the story than aba. *Plant physiology* **176**, 851–864, https://doi.org/10.1104/pp.17.00912 (2018).
16. Schönbeck, L. C. *et al*. Increasing temperature and vapour pressure deficit lead to hydraulic damages in the absence of soil drought. *Plant, Cell & Environment* **45**, 3275–3289, https://doi.org/10.1111/pce.14425 (2022).
17. Anderegg, W. R., Kane, J. M. & Anderegg, L. D. Consequences of widespread tree mortality triggered by drought and temperature stress. *Nature climate change* **3**, 30–36, https://doi.org/10.1038/nclimate1635 (2013).
18. Corak, N. K., Otkin, J. A., Ford, T. W. & Lowman, L. E. Unraveling phenological and stomatal responses to flash drought and implications for water and carbon budgets. *Hydrology and Earth System Sciences* **28**, 1827–1851, https://doi.org/10.5194/hess-28-1827-2024 (2024).

19. Zhang, S., Tao, F. & Zhang, Z. Spatial and temporal changes in vapor pressure deficit and their impacts on crop yields in china during 1980–2008. *Journal of Meteorological Research* **31**, 800–808, https://doi.org/10.1007/s13351-017-6137-z (2017).
20. Kern, A. *et al*. Statistical modelling of crop yield in central europe using climate data and remote sensing vegetation indices. *Agricultural and forest meteorology* **260**, 300–320, https://doi.org/10.1016/j.agrformet.2018.06.009 (2018).
21. Lobell, D. B. *et al*. The shifting influence of drought and heat stress for crops in northeast australia. *Global change biology* **21**, 4115–4127, https://doi.org/10.1111/gcb.13022 (2015).
22. Hsiao, J., Swann, A. L. & Kim, S.-H. Maize yield under a changing climate: The hidden role of vapor pressure deficit. *Agricultural and Forest Meteorology* **279**, 107692, https://doi.org/10.1016/j.agrformet.2019.107692 (2019).
23. Rashid, M. A., Andersen, M. N., Wollenweber, B., Zhang, X. & Olesen, J. E. Acclimation to higher vpd and temperature minimized negative effects on assimilation and grain yield of wheat. *Agricultural and forest meteorology* **248**, 119–129, https://doi.org/10.1016/j.agrformet.2017.09.018 (2018).
24. Seager, R. *et al*. Climatology, variability, and trends in the us vapor pressure deficit, an important fire-related meteorological quantity. *Journal of Applied Meteorology and Climatology* **54**, 1121–1141, https://doi.org/10.1175/JAMC-D-14-0321.1 (2015).
25. Chiodi, A. M., Potter, B. E. & Larkin, N. K. Multi-decadal change in western us nighttime vapor pressure deficit. *Geophysical Research Letters* **48**, e2021GL092830, https://doi.org/10.1029/2021GL092830 (2021).
26. Williams, A. P. *et al*. Observed impacts of anthropogenic climate change on wildfire in california. *Earth's Future* **7**, 892–910, https://doi.org/10.1029/2019EF001210 (2019).
27. Gonzalez, P., Neilson, R. P., Lenihan, J. M. & Drapek, R. J. Global patterns in the vulnerability of ecosystems to vegetation shifts due to climate change. *Global Ecology and Biogeography* **19**, 755–768, https://doi.org/10.1111/j.1466-8238.2010.00558.x (2010).
28. Williams, A. P. *et al*. Causes and implications of extreme atmospheric moisture demand during the record-breaking 2011 wildfire season in the southwestern united states. *Journal of Applied Meteorology and Climatology* **53**, 2671–2684, https://doi.org/10.1175/JAMC-D-14-0053.1 (2014).
29. Holden, Z. A. *et al*. Decreasing fire season precipitation increased recent western us forest wildfire activity. *Proceedings of the National Academy of Sciences* **115**, E8349–E8357, https://doi.org/10.1073/pnas.1802316115 (2018).
30. Littell, J. S., Peterson, D. L., Riley, K. L., Liu, Y. & Luce, C. H. A review of the relationships between drought and forest fire in the united states. *Global change biology* **22**, 2353–2369, https://doi.org/10.1111/gcb.13275 (2016).
31. Mitchell, R. J. *et al*. Future climate and fire interactions in the southeastern region of the united states. *Forest Ecology and Management* **327**, 316–326, https://doi.org/10.1016/j.foreco.2013.12.003 (2014).
32. Clarke, H. *et al*. Forest fire threatens global carbon sinks and population centres under rising atmospheric water demand. *Nature communications* **13**, 7161, https://doi.org/10.1038/s41467-022-34966-3 (2022).
33. Dingman, S. L. *Physical hydrology* (Waveland press, 2015).
34. Abtew, W. & Melesse, A. *Vapor Pressure Calculation Methods*, 53–62 (Springer Netherlands, Dordrecht, 2013).
35. Anderson, D. B. Relative humidity or vapor pressure deficit. *Ecology* **17**, 277–282, https://doi.org/10.2307/1931468 (1936).
36. Jensen, M. E. Consumptive use of water and irrigation water requirements. American Society of Civil Engineers (1974).
37. Castellvi, F., Perez, P., Villar, J. & Rosell, J. Analysis of methods for estimating vapor pressure deficits and relative humidity. *Agricultural and Forest Meteorology* **82**, 29–45, https://doi.org/10.1016/0168-1923(96)02343-X (1996).
38. Zhang, Q. *et al*. Response of ecosystem intrinsic water use efficiency and gross primary productivity to rising vapor pressure deficit. *Environmental Research Letters* **14**, 074023, https://doi.org/10.1088/1748-9326/ab2603 (2019).
39. Howell, T. A. & Dusek, D. A. Comparison of vapor-pressure-deficit calculation methods—southern high plains. *Journal of irrigation and drainage engineering* **121**, 191–198, https://doi.org/10.1061/(ASCE)0733-9437(1995)121:2(191) (1995).
40. Zhang, H., Wu, B., Yan, N., Zhu, W. & Feng, X. An improved satellite-based approach for estimating vapor pressure deficit from modis data. *Journal of Geophysical Research: Atmospheres* **119**, 12–256, https://doi.org/10.1002/2014JD022118 (2014).
41. Barkhordarian, A., Saatchi, S. S., Behrangi, A., Loikith, P. C. & Mechoso, C. R. A recent systematic increase in vapor pressure deficit over tropical south america. *Scientific reports* **9**, 15331, https://doi.org/10.1038/s41598-019-51857-8 (2019).
42. Baldocchi, D. *et al*. Fluxnet: A new tool to study the temporal and spatial variability of ecosystem-scale carbon dioxide, water vapor, and energy flux densities. *Bulletin of the American Meteorological Society* **82**, 2415–2434, https://doi.org/10.1175/1520-0477(2001)082 (2001).
43. Yang, F. *et al*. Assessing the representativeness of the ameriflux network using modis and goes data. *Journal of Geophysical Research: Biogeosciences* **113**, https://doi.org/10.1029/2007JG000627 (2008).
44. Novick, K. A. *et al*. The ameriflux network: A coalition of the willing. *Agricultural and Forest Meteorology* **249**, 444–456, https://doi.org/10.1016/j.agrformet.2017.10.009 (2018).
45. Hersbach, H. *et al*. The era5 global reanalysis. *Quarterly Journal of the Royal Meteorological Society* **146**, 1999–2049, https://doi.org/10.1002/qj.3803 (2020).
46. Fang, Z., Zhang, W., Brandt, M., Abdi, A. M. & Fensholt, R. Globally increasing atmospheric aridity over the 21st century. *Earth's future* **10**, e2022EF003019, https://doi.org/10.1029/2022EF003019 (2022).
47. Chu, H. *et al*. Representativeness of eddy-covariance flux footprints for areas surrounding ameriflux sites. *Agricultural and Forest Meteorology* **301-302**, 108350, https://doi.org/10.1016/j.agrformet.2021.108350 (2021).
48. Ficklin, D. L. & Novick, K. A. Historic and projected changes in vapor pressure deficit suggest a continental-scale drying of the united states atmosphere. *Journal of Geophysical Research: Atmospheres* **122**, 2061–2079, https://doi.org/10.1002/2016JD025855 (2017).
49. Sulman, B. N. *et al*. High atmospheric demand for water can limit forest carbon uptake and transpiration as severely as dry soil. *Geophysical Research Letters* **43**, 9686–9695, https://doi.org/10.1002/2016GL069416 (2016).
50. Gamelin, B. L. *et al*. Projected us drought extremes through the twenty-first century with vapor pressure deficit. *Scientific Reports* **12**, 8615, https://doi.org/10.1038/s41598-022-12516-7 (2022).
51. Chang, Q. *et al*. Earlier ecological drought detection by involving the interaction of phenology and eco-physiological function. *Earth's Future* **11**, e2022EF002667, https://doi.org/10.1029/2022EF002667 (2023).
52. McDonald, J. M., Srock, A. F. & Charney, J. J. Development and application of a hot-dry-windy index (hdw) climatology. *Atmosphere* **9**, 285, https://doi.org/10.3390/atmos9070285 (2018).
53. Hiraga, Y. & Kavvas, M. L. Hydrological and meteorological controls on large wildfire ignition and burned area in northern california during 2017–2020. *Fire* **4**, 90, https://doi.org/10.3390/fire4040090 (2021).
54. Thornton, M. *et al*. Daymet: Daily surface weather data on a 1-km grid for north america, version 4 r1. ORNL DAAC, Oak Ridge, Tennessee, USA https://doi.org/10.3334/ORNLDAAC/2129 (2022).
55. Sadler, E. J. & Evans, D. E. Vapor pressure deficit calculations and their effect on the combination equation. *Agricultural and Forest Meteorology* **49**, 55–80, https://doi.org/10.1016/0168-1923(89)90062-2 (1989).
56. Ghanem, M. E., Kehel, Z., Marrou, H. & Sinclair, T. R. Seasonal and climatic variation of weighted vpd for transpiration estimation. *European Journal of Agronomy* **113**, 125966, https://doi.org/10.1016/j.eja.2019.125966 (2020).
57. Thornton, P. E., Running, S. W. & White, M. A. Generating surfaces of daily meteorological variables over large regions of complex terrain. *Journal of hydrology* **190**, 214–251, https://doi.org/10.1016/S0022-1694(96)03128-9 (1997).
58. Thornton, P. E. *et al*. Gridded daily weather data for north america with comprehensive uncertainty quantification. *Scientific Data* **8**, 190, https://doi.org/10.1038/s41597-021-00973-0 (2021).

59. Thornton, P. E. & Running, S. W. An improved algorithm for estimating incident daily solar radiation from measurements of temperature, humidity, and precipitation. *Agricultural and forest meteorology* **93**, 211–228, https://doi.org/10.1016/S0168-1923(98)00126-9 (1999).
60. Thornton, P. E., Hasenauer, H. & White, M. A. Simultaneous estimation of daily solar radiation and humidity from observed temperature and precipitation: an application over complex terrain in austria. *Agricultural and forest meteorology* **104**, 255–271, https://doi.org/10.1016/S0168-1923(00)00170-2 (2000).
61. Kimball, J. S., Running, S. W. & Nemani, R. An improved method for estimating surface humidity from daily minimum temperature. *Agricultural and forest meteorology* **85**, 87–98, https://doi.org/10.1016/S0168-1923(96)02366-0 (1997).
62. Baldocchi, D., Valentini, R., Running, S., Oechel, W. & Dahlman, R. Strategies for measuring and modelling carbon dioxide and water vapour fluxes over terrestrial ecosystems. *Global change biology* **2**, 159–168, https://doi.org/10.1111/j.1365-2486.1996.tb00069.x (1996).
63. Friedl, M. & Sulla-Menashe, D. Modis/terra + aqua land cover type yearly l3 global 500 m sin grid v061 [data set], https://doi.org/10.5067/MODIS/MCD12Q1.061 Accessed 2023-06-01 (2022).
64. AppEEARS Team. Application for extracting and exploring analysis ready samples (appeears) https://appeears.earthdatacloud.nasa.gov. Accessed September 9, 2024. (2024).
65. Beck, H. E. *et al*. Present and future köppen-geiger climate classification maps at 1-km resolution. *Scientific data* **5**, 1–12, https://doi.org/10.1038/sdata.2018.214 (2018).
66. Beck, H. E. *et al*. Present and future köppen-geiger climate classification maps at 1-km resolution. *figshare*, https://doi.org/10.6084/m9.figshare.6396959 Dataset (2018).
67. Peel, M. C., Finlayson, B. L. & McMahon, T. A. Updated world map of the köppen-geiger climate classification. *Hydrology and earth system sciences* **11**, 1633–1644, https://doi.org/10.5194/hess-11-1633-2007 (2007).
68. Xia, Y. *et al*. Continental-scale water and energy flux analysis and validation for the north american land data assimilation system project phase 2 (nldas-2): 1. intercomparison and application of model products. *Journal of Geophysical Research: Atmospheres* **117**, https://doi.org/10.1029/2011JD016048 (2012).
69. Cosgrove, B. A. *et al*. Real-time and retrospective forcing in the north american land data assimilation system (nldas) project. *Journal of Geophysical Research: Atmospheres* **108**, https://doi.org/10.1029/2002JD003118 (2003).
70. Xia, Y. *et al*. NLDAS Primary Forcing Data L4 Hourly 0.125 × 0.125 degree V002, https://doi.org/10.5067/6J5LHHOHZHN4 Accessed: September 18, 2024 (2009).
71. Monteith, J. & Unsworth, M. *Principles of environmental physics: plants, animals, and the atmosphere* (Academic Press, 2013).
72. Junzeng, X., Qi, W., Shizhang, P. & Yanmei, Y. Error of saturation vapor pressure calculated by different formulas and its effect on calculation of reference evapotranspiration in high latitude cold region. *Procedia Engineering* **28**, 43–48, https://doi.org/10.1016/j.proeng.2012.01.680 (2012).
73. Running, S. W., Nemani, R. R. & Hungerford, R. D. Extrapolation of synoptic meteorological data in mountainous terrain and its use for simulating forest evapotranspiration and photosynthesis. *Canadian Journal of Forest Research* **17**, 472–483, https://doi.org/10.1139/x87-081 (1987).
74. Corak, N. K. & Lowman, L. E. L. Land cover and climate informed vapor pressure deficit datasets derived from daymet https://doi.org/10.4211/hs.de74b0a457c74deca09f9a41afa03c8f (2025).
75. Entekhabi, D., Reichle, R. H., Koster, R. D. & Crow, W. T. Performance metrics for soil moisture retrievals and application requirements. *Journal of Hydrometeorology* **11**, 832–840, https://doi.org/10.1175/2010JHM1223.1 (2010).
76. Otkin, J. A. *et al*. Flash droughts: A review and assessment of the challenges imposed by rapid-onset droughts in the united states. *Bulletin of the American Meteorological Society* **99**, 911–919, https://doi.org/10.1175/BAMS-D-17-0149.1 (2018).
77. Li, C. *et al*. Influence of vapor pressure deficit on vegetation growth in china. *Journal of Arid Land* 1–19, https://doi.org/10.1007/s40333-024-0077-0 (2024).
78. Anderson, M. C. *et al*. Evaluation of drought indices based on thermal remote sensing of evapotranspiration over the continental united states. *Journal of Climate* **24**, 2025–2044, https://doi.org/10.1175/2010JCLI3812.1 (2011).
79. Mahrt, L. & Ek, M. The influence of atmospheric stability on potential evaporation. *Journal of Applied Meteorology and Climatology* **23**, 222–234, https://doi.org/10.1175/1520-0450(1984)023 (1984).
80. Basara, J. B. *et al*. The evolution, propagation, and spread of flash drought in the central united states during 2012. *Environmental Research Letters* **14**, 084025, https://doi.org/10.1088/1748-9326/ab2cc0 (2019).
81. Sanginés de Cárcer, P. *et al*. Vapor–pressure deficit and extreme climatic variables limit tree growth. *Global Change Biology* **24**, 1108–1122, https://doi.org/10.1111/gcb.13973 (2018).
82. Ibanez, T. *et al*. Altered cyclone–fire interactions are changing ecosystems. *Trends in Plant Science* **27**, 1218–1230, https://doi.org/10.1016/j.tplants.2022.08.005 (2022).
83. Harris, I., Osborn, T. J., Jones, P. & Lister, D. Version 4 of the cru ts monthly high-resolution gridded multivariate climate dataset. *Scientific data* **7**, 109 (2020).
84. Information Systems and Wake Forest University. WFU High Performance Computing Facility, https://doi.org/10.57682/G13Z-2362 (2021).
85. Black, T. A. Ameriflux base ca-ca3 british columbia - pole sapling douglas-fir stand, ver. 6-5, https://doi.org/10.17190/AMF/1480302 (2023).
86. Knox, S. Ameriflux base ca-dsm delta salt marsh, ver. 1-5, https://doi.org/10.17190/AMF/1964085 (2023).
87. Wagner-Riddle, C. Ameriflux base ca-er1 elora research station, ver. 3-5, https://doi.org/10.17190/AMF/1579541 (2021).
88. McCaughey, J., Pejam, M., Arain, M. & Cameron, D. Carbon dioxide and energy fluxes from a boreal mixedwood forest ecosystem in ontario, canada, https://doi.org/10.1016/J.AGRFORMET.2006.08.010 (2006).
89. Bergeron, O. *et al*. Comparison of carbon dioxide fluxes over three boreal black spruce forests in canada, https://doi.org/10.1111/J.1365-2486.2006.01281.X (2006).
90. Peichl, M., Brodeur, J. J., Khomik, M. & Arain, M. A. Biometric and eddy-covariance based estimates of carbon fluxes in an age-sequence of temperate pine forests, https://doi.org/10.1016/J.AGRFORMET.2010.03.002 (2010).
91. Arain, M. A. Ameriflux base ca-tp2 ontario - turkey point 1989 plantation white pine, ver. 2-5, https://doi.org/10.17190/AMF/1246010 (2018).
92. Arain, M. A. & Restrepo-Coupe, N. Net ecosystem production in a temperate pine plantation in southeastern canada, https://doi.org/10.1016/J.AGRFORMET.2004.10.003 (2005).
93. Arain, M. A. Ameriflux base ca-tpd ontario - turkey point mature deciduous, ver. 2-5, https://doi.org/10.17190/AMF/1246152 (2018).
94. Yepez, E. A. Ameriflux base mx-aog alamos old-growth tropical dry forest, ver. 1-5, https://doi.org/10.17190/AMF/1756414 (2020).
95. Yepez, E. A. & Garatuza, J. Ameriflux base mx-tes tesopaco, secondary tropical dry forest, ver. 2-5, https://doi.org/10.17190/AMF/1767832 (2021).
96. Waldo, S. Ameriflux base us-act acton lake flux tower site, ver. 1-5, https://doi.org/10.17190/AMF/1846660 (2022).
97. Moreo, M. Ameriflux base us-adr amargosa desert research site (adrs), ver. 1-5, https://doi.org/10.17190/AMF/1418680 (2018).
98. Leclerc, M. Ameriflux base us-akn savannah river site, ver. 6-5, https://doi.org/10.17190/AMF/1246141 (2023).
99. Olson, B. Ameriflux base us-alq allequash creek site, ver. 18-5, https://doi.org/10.17190/AMF/1480323 (2024).

100. Billesbach, D., Bradford, J. & Torn, M. Ameriflux base us-ar1 arm usda unl osu woodward switchgrass 1, ver. 3-5, https://doi.org/10.17190/AMF/1246137 (2019).
101. Billesbach, D., Bradford, J. & Torn, M. Ameriflux base us-ar2 arm usda unl osu woodward switchgrass 2, ver. 3-5, https://doi.org/10.17190/AMF/1246138 (2019).
102. Torn, M. Ameriflux base us-arb arm southern great plains burn site- lamont, ver. 3-5, https://doi.org/10.17190/AMF/1246025 (2019).
103. Torn, M. Ameriflux base us-arc arm southern great plains control site- lamont, ver. 3-5, https://doi.org/10.17190/AMF/1246026 (2019).
104. Anderson, R. G. Ameriflux base us-ash ussl san joaquin valley almond high salinity, ver. 1-5, https://doi.org/10.17190/AMF/1634880 (2020).
105. Anderson, R. G. Ameriflux base us-asl ussl san joaquin valley almond low salinity, ver. 1-5, https://doi.org/10.17190/AMF/1617706 (2020).
106. Anderson, R. G. Ameriflux base us-asm ussl san joaquin valley almond medium salinity, ver. 1-5, https://doi.org/10.17190/AMF/1617709 (2020).
107. Ouimette, A. P. *et al*. Carbon fluxes and interannual drivers in a temperate forest ecosystem assessed through comparison of top-down and bottom-up approaches, https://doi.org/10.1016/J.AGRFORMET.2018.03.017 (2018).
108. Hemes, K. S. *et al*. Assessing the carbon and climate benefit of restoring degraded agricultural peat soils to managed wetlands, https://doi.org/10.1016/J.AGRFORMET.2019.01.017 (2019).
109. Rey-Sanchez, C. *et al*. Ameriflux base us-bi2 bouldin island corn, ver. 17-5, https://doi.org/10.17190/AMF/1419513 (2024).
110. Goldstein, A. Ameriflux base us-blo blodgett forest, ver. 4-5, https://doi.org/10.17190/AMF/1246032 (2019).
111. Meyers, T. Ameriflux base us-bo1 bondville, ver. 2-1, https://doi.org/10.17190/AMF/1246036 (2016).
112. Bernacchi, C. Ameriflux base us-bo2 bondville (companion site), ver. 2-1, https://doi.org/10.17190/AMF/1246037 (2016).
113. Davis, K. Ameriflux base us-bwa influx - nist turfgrass site, ver. 1-5, https://doi.org/10.17190/AMF/2229153 (2023).
114. Davis, K. Ameriflux base us-bwb influx - montgomery county pasture site, ver. 1-5, https://doi.org/10.17190/AMF/2229154 (2023).
115. Stoy, P. & Brevert, S. Ameriflux base us-cc1 coloma corn 1, ver. 1-5, https://doi.org/10.17190/AMF/1865475 (2022).
116. Bowling, D., Kannenberg, S. & Anderegg, W. Ameriflux base us-cdm cedar mesa, ver. 2-5, https://doi.org/10.17190/AMF/1865477 (2024).
117. Clark, K. Ameriflux base us-ced cedar bridge, ver. 7-1, https://doi.org/10.17190/AMF/1246043 (2016).
118. Phillips, C. L. & Huggins, D. Ameriflux base us-cf1 caf-ltar cook east, ver. 3-5, https://doi.org/10.17190/AMF/1543382 (2022).
119. Huggins, D. Ameriflux base us-cf2 caf-ltar cook west, ver. 2-5, https://doi.org/10.17190/AMF/1543383 (2021).
120. Huggins, D. Ameriflux base us-cf3 caf-ltar boyd north, ver. 3-5, https://doi.org/10.17190/AMF/1543385 (2022).
121. Huggins, D. Ameriflux base us-cf4 caf-ltar boyd south, ver. 3-5, https://doi.org/10.17190/AMF/1543384 (2022).
122. Bowling, D. Ameriflux base us-cop corral pocket, ver. 2-5, https://doi.org/10.17190/AMF/1246129 (2019).
123. Ewers, B., Bretfeld, M. & Pendall, E. Ameriflux base us-cpk chimney park, ver. 2-1, https://doi.org/10.17190/AMF/1246150 (2016).
124. Noormets, A. Ameriflux base us-crk davy crockett national forest, ver. 5-5, https://doi.org/10.17190/AMF/2204055 (2024).
125. Desai, A. Ameriflux base us-cs1 central sands irrigated agricultural field, ver. 3-5, https://doi.org/10.17190/AMF/1617710 (2023).
126. Desai, A. Ameriflux base us-cs2 tri county school pine forest, ver. 5-5, https://doi.org/10.17190/AMF/1617711 (2023).
127. Desai, A. Ameriflux base us-cs3 central sands irrigated agricultural field, ver. 4-5, https://doi.org/10.17190/AMF/1617713 (2023).
128. Desai, A. Ameriflux base us-cs4 central sands irrigated agricultural field, ver. 4-5, https://doi.org/10.17190/AMF/1756417 (2023).
129. Desai, A. Ameriflux base us-cs5 central sands irrigated agricultural field, ver. 1-5, https://doi.org/10.17190/AMF/1846663 (2022).
130. Desai, A. Ameriflux base us-cs6 central sands irrigated agricultural field, ver. 1-5, https://doi.org/10.17190/AMF/2001297 (2023).
131. Desai, A. Ameriflux base us-cs8 central sands irrigated agricultural field, ver. 2-5, https://doi.org/10.17190/AMF/2001298 (2023).
132. Novick, K. Ameriflux base us-cst crossett experimental forest, ver. 1-5, https://doi.org/10.17190/AMF/1902275 (2022).
133. Oishi, A. C. Ameriflux base us-cwt coweeta, ver. 1-5, https://doi.org/10.17190/AMF/1671890 (2020).
134. Duff, A. & Desai, A. Ameriflux base us-dfc us dairy forage research center, prairie du sac, ver. 2-5, https://doi.org/10.17190/AMF/1660340 (2023).
135. Duff, A., Desai, A. & Risso, V. P. Ameriflux base us-dfk dairy forage research center - kernza, ver. 1-5, https://doi.org/10.17190/AMF/1825937 (2021).
136. DuBois, S. *et al*. Using imaging spectroscopy to detect variation in terrestrial ecosystem productivity across a water-stressed landscape, https://doi.org/10.1002/EAP.1733 (2018).
137. Clark, K. Ameriflux base us-dix fort dix, ver. 2-1, https://doi.org/10.17190/AMF/1246045 (2016).
138. Oishi, C., Novick, K. & Stoy, P. Ameriflux base us-dk1 duke forest-open field, ver. 4-5, https://doi.org/10.17190/AMF/1246046 (2018).
139. Oishi, C., Novick, K. & Stoy, P. Ameriflux base us-dk2 duke forest-hardwoods, ver. 4-5, https://doi.org/10.17190/AMF/1246047 (2018).
140. Oishi, C., Novick, K. & Stoy, P. Ameriflux base us-dk3 duke forest - loblolly pine, ver. 4-5, https://doi.org/10.17190/AMF/1246048 (2018).
141. Arias-Ortiz, A. & Baldocchi, D. Ameriflux base us-dmg dutch slough marsh gilbert tract, ver. 2-5, https://doi.org/10.17190/AMF/1964086 (2024).
142. Hinkle, C. R. & Bracho, R. Ameriflux base us-dpw disney wilderness preserve wetland, ver. 1-5, https://doi.org/10.17190/AMF/1562387 (2019).
143. McKinney, T. Ameriflux base us-ea4 eaa field research park woodland, ver. 1-5, https://doi.org/10.17190/AMF/2315767 (2024).
144. McKinney, T. Ameriflux base us-ea5 uvalde ranch mesquite woodland, ver. 2-5, https://doi.org/10.17190/AMF/2204056 (2024).
145. McKinney, T. Ameriflux base us-ea6 camp wood shield ranch oak savannah, ver. 1-5, https://doi.org/10.17190/AMF/2315768 (2024).
146. Oikawa, P. Ameriflux base us-edn eden landing ecological reserve, ver. 2-5, https://doi.org/10.17190/AMF/1543381 (2020).
147. Starr, G. & Oberbauer, S. Ameriflux base us-elm everglades (long hydroperiod marsh), ver. 4-1, https://doi.org/10.17190/AMF/1246118 (2016).
148. Starr, G. & Oberbauer, S. Ameriflux base us-esm everglades (short hydroperiod marsh), ver. 5-1, https://doi.org/10.17190/AMF/1246119 (2016).
149. Starr, G. & Oberbuer, S. F. Ameriflux base us-evm everglades saltwater intrusion marsh, ver. 2-5, https://doi.org/10.17190/AMF/2229155 (2024).
150. Dore, S. & Kolb, T. Ameriflux base us-fmf flagstaff - managed forest, ver. 6-5, https://doi.org/10.17190/AMF/1246050 (2019).
151. Dore, S. & Kolb, T. Ameriflux base us-fuf flagstaff - unmanaged forest, ver. 6-5, https://doi.org/10.17190/AMF/1246051 (2019).
152. Dore, S. & Kolb, T. Ameriflux base us-fwf flagstaff - wildfire, ver. 8-5, https://doi.org/10.17190/AMF/1246052 (2019).
153. Massman, B. Ameriflux base us-gbt glees brooklyn tower, ver. 1-1, https://doi.org/10.17190/AMF/1375200 (2016).
154. Spence, C. Ameriflux base us-gl1 stannard rock, ver. 3-5, https://doi.org/10.17190/AMF/2204057 (2024).
155. Frank, J. M., Massman, W. J., Ewers, B. E., Huckaby, L. S. & Negrón, J. F. Ecosystem CO_2/H_2O fluxes are explained by hydraulically limited gas exchange during tree mortality from spruce bark beetles, https://doi.org/10.1002/2013JG002597 (2014).
156. Hadley, J. & Munger, J. W. Ameriflux base us-ha2 harvard forest hemlock site, ver. 12-5, https://doi.org/10.17190/AMF/1246060 (2024).

157. Forsythe, J. D., O'Halloran, T. L. & Kline, M. A. An eddy covariance mesonet for measuring greenhouse gas fluxes in coastal south carolina, https://doi.org/10.3390/DATA5040097 (2020).
158. O'Halloran, T. Ameriflux base us-hb4 minim creek brackish impoundment, ver. 1-5, https://doi.org/10.17190/AMF/2001299 (2023).
159. Kelsey, E. & Green, M. Ameriflux base us-hbk hubbard brook experimental forest, ver. 2-5, https://doi.org/10.17190/AMF/1634881 (2023).
160. Hollinger, D. Ameriflux base us-ho1 howland forest (main tower), ver. 9-5, https://doi.org/10.17190/AMF/1246061 (2024).
161. Hollinger, D. Ameriflux base us-ho2 howland forest (west tower), ver. 6-5, https://doi.org/10.17190/AMF/1246062 (2024).
162. Hollinger, D. Ameriflux base us-ho3 howland forest (harvest site), ver. 2-1, https://doi.org/10.17190/AMF/1246063 (2016).
163. Arias-Ortiz, A., Szutu, D., Verfaillie, J. & Baldocchi, D. Ameriflux base us-hsm hill slough marsh, ver. 4-5, https://doi.org/10.17190/AMF/1890483 (2024).
164. Davis, K. Ameriflux base us-ina influx - cemetery turfgrass tower, ver. 1-5, https://doi.org/10.17190/AMF/2001300 (2023).
165. Davis, K. Ameriflux base us-inb influx - golf course, ver. 1-5, https://doi.org/10.17190/AMF/2001301 (2023).
166. Davis, K. Ameriflux base us-inc influx - downtown indianapolis (site-3), ver. 2-5, https://doi.org/10.17190/AMF/1987603 (2023).
167. Davis, K. Ameriflux base us-ind influx - agricultural site east near pittsboro, ver. 1-5, https://doi.org/10.17190/AMF/2001302 (2023).
168. Davis, K. Ameriflux base us-ine influx - agricultural site west near pittsboro, ver. 1-5, https://doi.org/10.17190/AMF/2001303 (2023).
169. Forsythe, B. R., Horne, J. & Davis, K. Ameriflux base us-ing influx - wayne twp comm (site-7), ver. 1-5, https://doi.org/10.17190/AMF/2001305 (2023).
170. Davis, K. Ameriflux base us-ini influx - agricultural site east of indianapolis (site-9a), ver. 1-5, https://doi.org/10.17190/AMF/2001306 (2023).
171. Davis, K. Ameriflux base us-inj influx - agricultural site east of indianapolis (site-9b), ver. 1-5, https://doi.org/10.17190/AMF/2001307 (2023).
172. Davis, K. Ameriflux base us-inn influx - agricultural site west of indianapolis (site-14a), ver. 1-5, https://doi.org/10.17190/AMF/2001308 (2023).
173. Davis, K. Ameriflux base us-inp influx - agricultural site west of indianapolis (site-14b), ver. 1-5, https://doi.org/10.17190/AMF/2001309 (2023).
174. Schreiner-McGraw, A. P. & Vivoni, E. R. Percolation observations in an arid piedmont watershed and linkages to historical conditions in the chihuahuan desert, https://doi.org/10.1002/ECS2.2000 (2017).
175. Brunsell, N. Ameriflux base us-kfs kansas field station, ver. 7-5, https://doi.org/10.17190/AMF/1246132 (2020).
176. Robertson, G. P. & Chen, J. Ameriflux base us-kl1 kbs lux arbor reserve corn, ver. 3-5, https://doi.org/10.17190/AMF/1660344 (2022).
177. Robertson, G. P. & Chen, J. Ameriflux base us-kl2 kbs lux arbor reserve switchgrass, ver. 4-5, https://doi.org/10.17190/AMF/1644212 (2022).
178. Robertson, G. P. & Chen, J. Ameriflux base us-kl3 kbs lux arbor reserve prairie, ver. 4-5, https://doi.org/10.17190/AMF/1647438 (2022).
179. Brunsell, N. Ameriflux base us-kls kansas land institute, ver. 2-5, https://doi.org/10.17190/AMF/1498745 (2021).
180. Robertson, G. P. & Chen, J. Ameriflux base us-km1 kbs marshall farms corn, ver. 4-5, https://doi.org/10.17190/AMF/1647439 (2022).
181. Robertson, G. P. & Chen, J. Ameriflux base us-km2 kbs marshall farms prairie, ver. 4-5, https://doi.org/10.17190/AMF/1647440 (2022).
182. Robertson, G. P. & Chen, J. Ameriflux base us-km3 kbs marshall farms switchgrass, ver. 3-5, https://doi.org/10.17190/AMF/1660345 (2022).
183. Robertson, G. P. & Chen, J. Ameriflux base us-km4 kbs marshall farms smooth brome grass (ref), ver. 5-5, https://doi.org/10.17190/AMF/1634882 (2022).
184. Brunsell, N. Ameriflux base us-kon konza prairie lter (knz), ver. 5-5, https://doi.org/10.17190/AMF/1246068 (2020).
185. Drake, B., Hinkle, R., Bracho, R., Powell, T. & Dore, S. Ameriflux base us-ks1 kennedy space center (slash pine), ver. 3-5, https://doi.org/10.17190/AMF/1246069 (2019).
186. Drake, B., Hinkle, R., Bracho, R., Dore, S. & Powell, T. Ameriflux base us-ks2 kennedy space center (scrub oak), ver. 3-5, https://doi.org/10.17190/AMF/1246070 (2019).
187. Bracho, R. & Hinkle, C. R. Ameriflux base us-ks3 kennedy space center (salt marsh), ver. 1-5, https://doi.org/10.17190/AMF/1562390 (2019).
188. McFadden, J. Ameriflux base us-kut kuom turfgrass field, ver. 1-1, https://doi.org/10.17190/AMF/1246145 (2016).
189. Krauss, K. Ameriflux base us-la1 pointe-aux-chenes brackish marsh, ver. 2-5, https://doi.org/10.17190/AMF/1543386 (2019).
190. Ward, E., Merino, S., Stagg, C. & Krauss, K. Ameriflux base us-la2 salvador wma freshwater marsh, ver. 3-5, https://doi.org/10.17190/AMF/1543387 (2023).
191. Fares, S. Ameriflux base us-lin lindcove orange orchard, ver. 2-5, https://doi.org/10.17190/AMF/1246830 (2019).
192. Starr, G. Ameriflux base us-ll1 longleaf pine - baker (mesic site), ver. 2-5, https://doi.org/10.17190/AMF/1773395 (2021).
193. Starr, G. Ameriflux base us-ll2 longleaf pine - dubignion (intermediate site), ver. 1-5, https://doi.org/10.17190/AMF/1773396 (2021).
194. Starr, G. Ameriflux base us-ll3 longleaf pine - red dirt (xeric site), ver. 1-5, https://doi.org/10.17190/AMF/1773397 (2021).
195. Sulman, B. N., Desai, A. R., Cook, B. D., Saliendra, N. & Mackay, D. S. Contrasting carbon dioxide fluxes between a drying shrub wetland in northern wisconsin, usa, and nearby forests, https://doi.org/10.5194/BG-6-1115-2009 (2009).
196. Stoy, P. & Torrion, J. Ameriflux base us-mc1 creston, montana pivot-irrigated spring wheat, ver. 1-5, https://doi.org/10.17190/AMF/1660348 (2020).
197. Stoy, P. & Torrion, J. Ameriflux base us-mc2 creston, montana pivot-irrigated spring wheat 2, ver. 1-5, https://doi.org/10.17190/AMF/1829506 (2021).
198. Irvine, J., Law, B. E. & Hibbard, K. A. Postfire carbon pools and fluxes in semiarid ponderosa pine in central oregon, https://doi.org/10.1111/J.1365-2486.2007.01368.X (2007).
199. Law, B. Ameriflux base us-me4 metolius-old aged ponderosa pine, ver. 6-5, https://doi.org/10.17190/AMF/1246078 (2024).
200. Law, B. Ameriflux base us-me5 metolius-first young aged pine, ver. 3-5, https://doi.org/10.17190/AMF/1246079 (2021).
201. Desai, A. Ameriflux base us-men lake mendota, center for limnology site, ver. 3-5, https://doi.org/10.17190/AMF/1433375 (2018).
202. Stoy, P. & McVay, K. Ameriflux base us-mh1 huntley, montana irrigated barley site 1, ver. 1-5, https://doi.org/10.17190/AMF/1660349 (2020).
203. Stoy, P. & McVay, K. Ameriflux base us-mh2 huntley, montana irrigated barley site 2, ver. 1-5, https://doi.org/10.17190/AMF/1825938 (2021).
204. Vick, E. S., Stoy, P. C., Tang, A. C. & Gerken, T. The surface-atmosphere exchange of carbon dioxide, water, and sensible heat across a dryland wheat-fallow rotation, https://doi.org/10.1016/J.AGEE.2016.07.018 (2016).
205. Novick, K. & Phillips, R. Ameriflux base us-mms morgan monroe state forest, ver. 26-5, https://doi.org/10.17190/AMF/1246080 (2024).

206. Johnson, J. Ameriflux base us-mn1 morris: Corn-soybean with cover crops, strip tillage, ver. 1-5, https://doi.org/10.17190/AMF/2407204 (2024).
207. Johnson, J. Ameriflux base us-mn3 morris: Corn-soybean, conventional tillage, ver. 1-5, https://doi.org/10.17190/AMF/2407206 (2024).
208. Schreiner-McGraw, A. Ameriflux base us-mo1 ltar cmrb field 1 (cmrb asp), ver. 3-5, https://doi.org/10.17190/AMF/1870588 (2024).
209. Schreiner-McGraw, A. Ameriflux base us-mo2 ltar cmrb tucker prairie (cmrb tp), ver. 3-5, https://doi.org/10.17190/AMF/1902276 (2024).
210. Schreiner-McGraw, A. Ameriflux base us-mo3 ltar cmrb field 3 (cmrb bau), ver. 3-5, https://doi.org/10.17190/AMF/1870589 (2024).
211. Litvak, M. Ameriflux base us-mpj mountainair pinyon-juniper woodland, ver. 24-5, https://doi.org/10.17190/AMF/1246123 (2024).
212. Stoy, P. Ameriflux base us-msr montana sun river winter wheat, ver. 3-5, https://doi.org/10.17190/AMF/1617717 (2022).
213. Barron-Gafford, G. Ameriflux base us-mtb mt bigelow, ver. 4-5, https://doi.org/10.17190/AMF/1579717 (2022).
214. Stoy, P. Ameriflux base us-mvf montana vaughn fallow, ver. 1-5, https://doi.org/10.17190/AMF/1829507 (2021).
215. Stoy, P. Ameriflux base us-mvw montana vaughn wheat, ver. 1-5, https://doi.org/10.17190/AMF/1829508 (2021).
216. Matthes, J. H. *et al*. Ameriflux base us-myb mayberry wetland, ver. 14-5, https://doi.org/10.17190/AMF/1246139 (2024).
217. Domec, J.-C. *et al*. Interactive effects of nocturnal transpiration and climate change on the root hydraulic redistribution and carbon and water budgets of southern united states pine plantations, https://doi.org/10.1093/TREEPHYS/TPS018 (2012).
218. Noormets, A. *et al*. Ameriflux base us-nc3 nc_clearcut#3, ver. 4-5, https://doi.org/10.17190/AMF/1419506 (2022).
219. Noormets, A. *et al*. Ameriflux base us-nc4 nc_alligatorriver, ver. 5-5, https://doi.org/10.17190/AMF/1480314 (2022).
220. Chen, J. Ameriflux base us-nmj northern michigan jack pine stand, ver. 3-5, https://doi.org/10.17190/AMF/1246087 (2019).
221. Burns, S. P., Blanken, P. D., Turnipseed, A. A., Hu, J. & Monson, R. K. The influence of warm-season precipitation on the diel cycle of the surface energy balance and carbon dioxide at a colorado subalpine forest site, https://doi.org/10.5194/BG-12-7349-2015 (2015).
222. Knowles, J. Ameriflux base us-nr3 niwot ridge alpine (t-van west), ver. 5-5, https://doi.org/10.17190/AMF/1804491 (2024).
223. Knowles, J. Ameriflux base us-nr4 niwot ridge alpine (t-van east), ver. 5-5, https://doi.org/10.17190/AMF/1804492 (2024).
224. Silveira, M. L. & Bracho, R. Ameriflux base us-ona florida pine flatwoods, ver. 4-5, https://doi.org/10.17190/AMF/1660350 (2024).
225. Rey-Sanchez, A., Morin, T., Stefanik, K., Wrighton, K. & Bohrer, G. Determining total emissions and environmental drivers of methane flux in a lake erie estuarine marsh, https://doi.org/10.1016/J.ECOLENG.2017.06.042 (2018).
226. Bracho, R. & Silveira, M. L. Ameriflux base us-pas florida, paspalum notatum pasture, ver. 2-5, https://doi.org/10.17190/AMF/1870590 (2023).
227. Desai, A. R. *et al*. Landscape-level terrestrial methane flux observed from a very tall tower, https://doi.org/10.1016/J.AGRFORMET.2014.10.017 (2015).
228. Desai, A., Butterworth, B., Thom, J. & Stoy, P. Ameriflux base us-pff nw5 grass-1 cheesehead 2019, ver. 1-5, https://doi.org/10.17190/AMF/1890484 (2022).
229. Desai, A., Butterworth, B., Thom, J. & Stoy, P. Ameriflux base us-pfo se1 lake-2 cheesehead 2019, ver. 1-5, https://doi.org/10.17190/AMF/1880912 (2022).
230. Giblin, A. Ameriflux base us-phm plum island high marsh, ver. 3-5, https://doi.org/10.17190/AMF/1543377 (2021).
231. Desai, A. Ameriflux base us-pnp lake mendota, picnic point site, ver. 8-5, https://doi.org/10.17190/AMF/1433376 (2023).
232. Anderson, R. G. Ameriflux base us-psh ussl san joaquin valley pistachio high, ver. 1-5, https://doi.org/10.17190/AMF/1617719 (2020).
233. Anderson, R. G. Ameriflux base us-psl ussl san joaquin valley pistachio low, ver. 1-5, https://doi.org/10.17190/AMF/1617720 (2020).
234. Lamb, B. & Pressley, S. Ameriflux base us-rc1 cook agronomy farm - no till, ver. 2-5, https://doi.org/10.17190/AMF/1498748 (2021).
235. Lamb, B. & Pressley, S. Ameriflux base us-rc2 cook agronomy farm - conventional till, ver. 2-5, https://doi.org/10.17190/AMF/1498747 (2021).
236. Lamb, B. & Pressley, S. Ameriflux base us-rc3 wsu lind dryland research station, ver. 2-5, https://doi.org/10.17190/AMF/1498749 (2021).
237. Lamb, B. & Pressley, S. Ameriflux base us-rc4 moscow mountain on-farm site, ver. 2-5, https://doi.org/10.17190/AMF/1498750 (2021).
238. Lamb, B. & Pressley, S. Ameriflux base us-rc5 moses lake on-farm site, ver. 2-5, https://doi.org/10.17190/AMF/1498751 (2021).
239. Baker, J. & Griffis, T. Examining strategies to improve the carbon balance of corn/soybean agriculture using eddy covariance and mass balance techniques, https://doi.org/10.1016/J.AGRFORMET.2004.11.005 (2005).
240. Baker, J. & Griffis, T. Ameriflux base us-ro2 rosemount- c7, ver. 2-5, https://doi.org/10.17190/AMF/1418683 (2023).
241. Baker, J. & Griffis, T. Ameriflux base us-ro3 rosemount- g19, ver. 4-5, https://doi.org/10.17190/AMF/1246093 (2019).
242. Baker, J. & Griffis, T. Ameriflux base us-ro4 rosemount prairie, ver. 24-5, https://doi.org/10.17190/AMF/1419507 (2024).
243. Baker, J. & Griffis, T. Ameriflux base us-ro5 rosemount i18_south, ver. 24-5, https://doi.org/10.17190/AMF/1419508 (2024).
244. Baker, J. & Griffis, T. Ameriflux base us-ro6 rosemount i18_north, ver. 24-5, https://doi.org/10.17190/AMF/1419509 (2024).
245. Haber, L. & Poppe, K. Ameriflux base us-rrc rice rivers center marsh, ver. 1-5, https://doi.org/10.17190/AMF/2331382 (2024).
246. Billesbach, D. & Arkebauer, T. J. Ameriflux base us-sdh nebraska sandhills dry valley, ver. 1-1, https://doi.org/10.17190/AMF/1246136 (2016).
247. Litvak, M. Ameriflux base us-seg sevilleta grassland, ver. 24-5, https://doi.org/10.17190/AMF/1246124 (2024).
248. Litvak, M. Ameriflux base us-ses sevilleta shrubland, ver. 24-5, https://doi.org/10.17190/AMF/1246125 (2024).
249. Clark, K. Ameriflux base us-slt silas little- new jersey, ver. 5-1, https://doi.org/10.17190/AMF/1246096 (2016).
250. Hatala, J. A. *et al*. Greenhouse gas (co2, ch4, h2o) fluxes from drained and flooded agricultural peatlands in the sacramento-san joaquin delta, https://doi.org/10.1016/J.AGEE.2012.01.009 (2012).
251. Shortt, R., Hemes, K., Szutu, D., Verfaillie, J. & Baldocchi, D. Ameriflux base us-sne sherman island restored wetland, ver. 7-5, https://doi.org/10.17190/AMF/1418684 (2021).
252. Kusak, K., Sanchez, C. R., Szutu, D. & Baldocchi, D. Ameriflux base us-snf sherman barn, ver. 3-5, https://doi.org/10.17190/AMF/1579718 (2020).
253. Bracho, R. & Martin, T. A. Ameriflux base us-sp1 slashpine-austin cary- 65 yrs nat regen, ver. 5-5, https://doi.org/10.17190/AMF/1246100 (2023).
254. Bracho, R. & Martin, T. Ameriflux base us-sp2 slashpine-mize-clearcut-3yr,regen, ver. 3-1, https://doi.org/10.17190/AMF/1246101 (2016).
255. Bracho, R. & Martin, T. Ameriflux base us-sp3 slashpine-donaldson-mid-rot- 12 yrs, ver. 3-1, https://doi.org/10.17190/AMF/1246102 (2016).
256. Bracho, R. & Martin, T. A. Ameriflux base us-sp4 slashpine-rayonier-mid-rot- 12 yrs, ver. 3-5, https://doi.org/10.17190/AMF/1246103 (2019).
257. Kurc, S. Ameriflux base us-src santa rita creosote, ver. 6-5, https://doi.org/10.17190/AMF/1246127 (2019).

258. Bergamaschi, B. & Windham-Myers, L. Ameriflux base us-srr suisun marsh - rush ranch, ver. 1-5, https://doi.org/10.17190/AMF/1418685 (2018).
259. Anderson, C. A. & Vivoni, E. R. Impact of land surface states within the flux footprint on daytime land-atmosphere coupling in two semiarid ecosystems of the southwestern u.s., https://doi.org/10.1002/2015WR018016 (2016).
260. Ewers, B. & Pendall, E. Ameriflux base us-sta saratoga, ver. 2-5, https://doi.org/10.17190/AMF/1246831 (2019).
261. Vázquez-Lule, A. & Vargas, R. Biophysical drivers of net ecosystem and methane exchange across phenological phases in a tidal salt marsh, https://doi.org/10.1016/J.AGRFORMET.2020.108309 (2021).
262. Desai, A. R., Bolstad, P. V., Cook, B. D., Davis, K. J. & Carey, E. V. Comparing net ecosystem exchange of carbon dioxide between an old-growth and mature forest in the upper midwest, usa, https://doi.org/10.1016/J.AGRFORMET.2004.09.005 (2005).
263. Malone, S. & Troxler, T. Ameriflux base us-tas taylor slough/panhandle, ver. 1-5, https://doi.org/10.17190/AMF/2331383 (2024).
264. Stoy, P. Ameriflux base us-tef tenderfoot creek experimental forest, ver. 1-5, https://doi.org/10.17190/AMF/2315770 (2024).
265. Tree–grass interactions in savannas: Paradigms, contradictions, and conceptual models, https://doi.org/10.1201/B10275-10 (2010).
266. Stoy, P., Cook, A. & Dore, J. Ameriflux base us-tur turner ranch, ver. 1-5, https://doi.org/10.17190/AMF/1825940 (2021).
267. Valach, A. *et al*. Ameriflux base us-tw1 twitchell wetland west pond, ver. 11-5, https://doi.org/10.17190/AMF/1246147 (2024).
268. Sturtevant, C., Verfaillie, J. & Baldocchi, D. Ameriflux base us-tw2 twitchell corn, ver. 2-5, https://doi.org/10.17190/AMF/1246148 (2019).
269. Baldocchi, D., Sturtevant, C. & Contributors, F. Does day and night sampling reduce spurious correlation between canopy photosynthesis and ecosystem respiration?, https://doi.org/10.1016/J.AGRFORMET.2015.03.010 (2015).
270. Eichelmann, E. *et al*. Ameriflux base us-tw4 twitchell east end wetland, ver. 14-5, https://doi.org/10.17190/AMF/1246151 (2024).
271. Kasak, K. *et al*. Experimental harvesting of wetland plants to evaluate trade-offs between reducing methane emissions and removing nutrients accumulated to the biomass in constructed wetlands, https://doi.org/10.1016/J.SCITOTENV.2020.136960 (2020).
272. Blakely, B., Moore, C., Bernacchi, C. J. & Pederson, T. Ameriflux base us-uia university of illinois switchgrass, ver. 2-5, https://doi.org/10.17190/AMF/1617725 (2022).
273. Blakely, B., Moore, C., Bernacchi, C. J. & Pederson, T. Ameriflux base us-uib university of illinois miscanthus, ver. 2-5, https://doi.org/10.17190/AMF/1846664 (2023).
274. Bernacchi, C. J., Blakely, B., Moore, C. & Pederson, T. Ameriflux base us-uic university of illinois maize-soy, ver. 1-5, https://doi.org/10.17190/AMF/1846665 (2022).
275. Bernacchi, C. J. Ameriflux base us-uid university of illinois restored native prairie, ver. 1-5, https://doi.org/10.17190/AMF/1987605 (2023).
276. Bohrer, G. Ameriflux base us-um3 douglas lake, ver. 1-5, https://doi.org/10.17190/AMF/1480315 (2018).
277. Gough, C., Bohrer, G. & Curtis, P. Ameriflux base us-umb univ. of mich. biological station, ver. 21-5, https://doi.org/10.17190/AMF/1246107 (2024).
278. Ladig, K. & Inkenbrandt, P. Ameriflux base us-utb uflux bonneville salt flats, ver. 2-5, https://doi.org/10.17190/AMF/2001311 (2024).
279. Inkenbrandt, P. Ameriflux base us-utn uflux nephi, ver. 1-5, https://doi.org/10.17190/AMF/2204058 (2023).
280. Ma, S., Baldocchi, D. D., Xu, L. & Hehn, T. Inter-annual variability in carbon dioxide exchange of an oak/grass savanna and open grassland in california, https://doi.org/10.1016/J.AGRFORMET.2007.07.008 (2007).
281. Litvak, M. Ameriflux base us-vcm valles caldera mixed conifer, ver. 25-5, https://doi.org/10.17190/AMF/1246121 (2024).
282. Litvak, M. Ameriflux base us-vcp valles caldera ponderosa pine, ver. 23-5, https://doi.org/10.17190/AMF/1246122 (2024).
283. Litvak, M. Ameriflux base us-vcs valles caldera sulphur springs mixed conifer, ver. 16-5, https://doi.org/10.17190/AMF/1418681 (2024).
284. Cook, B. D. *et al*. Carbon exchange and venting anomalies in an upland deciduous forest in northern wisconsin, usa, https://doi.org/10.1016/J.AGRFORMET.2004.06.008 (2004).
285. Chen, J. Ameriflux base us-wi0 young red pine (yrp), ver. 3-5, https://doi.org/10.17190/AMF/1246016 (2020).
286. Chen, J. Ameriflux base us-wi1 intermediate hardwood (ihw), ver. 3-5, https://doi.org/10.17190/AMF/1246015 (2020).
287. Chen, J. Ameriflux base us-wi2 intermediate red pine (irp), ver. 3-5, https://doi.org/10.17190/AMF/1246017 (2020).
288. Chen, J. Ameriflux base us-wi3 mature hardwood (mhw), ver. 3-5, https://doi.org/10.17190/AMF/1246018 (2020).
289. Chen, J. Ameriflux base us-wi4 mature red pine (mrp), ver. 3-5, https://doi.org/10.17190/AMF/1246019 (2020).
290. Chen, J. Ameriflux base us-wi5 mixed young jack pine (myjp), ver. 3-5, https://doi.org/10.17190/AMF/1246020 (2020).
291. Chen, J. Ameriflux base us-wi6 pine barrens #1 (pb1), ver. 3-5, https://doi.org/10.17190/AMF/1246021 (2020).
292. Chen, J. Ameriflux base us-wi7 red pine clearcut (rpcc), ver. 3-5, https://doi.org/10.17190/AMF/1246022 (2020).
293. Chen, J. Ameriflux base us-wi8 young hardwood clearcut (yhw), ver. 3-5, https://doi.org/10.17190/AMF/1246023 (2020).
294. Chen, J. Ameriflux base us-wi9 young jack pine (yjp), ver. 3-5, https://doi.org/10.17190/AMF/1246024 (2020).
295. Litvak, M. Ameriflux base us-wjs willard juniper savannah, ver. 24-5, https://doi.org/10.17190/AMF/1246120 (2024).
296. Wharton, S. Ameriflux base us-wrc wind river crane site, ver. 8-1, https://doi.org/10.17190/AMF/1246114 (2016).
297. Bednarz, C. Ameriflux base us-wt1 kress, tx no-till cotton and grain sorghum production, ver. 1-5, https://doi.org/10.17190/AMF/2407207 (2024).
298. Network), N. N. E. O. Ameriflux base us-xab neon abby road (abby), ver. 9-5, https://doi.org/10.17190/AMF/1617726 (2024).
299. Network), N. N. E. O. Ameriflux base us-xae neon klemme range research station (oaes), ver. 8-5, https://doi.org/10.17190/AMF/1671891 (2024).
300. Network), N. N. E. O. Ameriflux base us-xbl neon blandy experimental farm (blan), ver. 8-5, https://doi.org/10.17190/AMF/1671893 (2024).
301. Network), N. N. E. O. Ameriflux base us-xbr neon bartlett experimental forest (bart), ver. 9-5, https://doi.org/10.17190/AMF/1579542 (2024).
302. Network), N. N. E. O. Ameriflux base us-xcl neon lbj national grassland (clbj), ver. 8-5, https://doi.org/10.17190/AMF/1671894 (2024).
303. Network), N. N. E. O. Ameriflux base us-xcp neon central plains experimental range (cper), ver. 9-5, https://doi.org/10.17190/AMF/1579720 (2024).
304. Network), N. N. E. O. Ameriflux base us-xdc neon dakota coteau field school (dcfs), ver. 9-5, https://doi.org/10.17190/AMF/1617728 (2024).
305. Network), N. N. E. O. Ameriflux base us-xdl neon dead lake (dela), ver. 9-5, https://doi.org/10.17190/AMF/1579721 (2024).
306. Network), N. N. E. O. Ameriflux base us-xds neon disney wilderness preserve (dsny), ver. 8-5, https://doi.org/10.17190/AMF/1671895 (2024).
307. Network), N. N. E. O. Ameriflux base us-xgr neon great smoky mountains national park, twin creeks (grsm), ver. 9-5, https://doi.org/10.17190/AMF/1634885 (2024).
308. Network), N. N. E. O. Ameriflux base us-xha neon harvard forest (harv), ver. 10-5, https://doi.org/10.17190/AMF/1562391 (2024).
309. Network), N. N. E. O. Ameriflux base us-xje neon jones ecological research center (jerc), ver. 9-5, https://doi.org/10.17190/AMF/1617730 (2024).
310. Network), N. N. E. O. Ameriflux base us-xjr neon jornada lter (jorn), ver. 9-5, https://doi.org/10.17190/AMF/1617731 (2024).

311. Network), N. N. E. O. Ameriflux base us-xka neon konza prairie biological station - relocatable (kona), ver. 9-5, https://doi.org/10.17190/AMF/1579722 (2024).
312. Network), N. N. E. O. Ameriflux base us-xkz neon konza prairie biological station (konz), ver. 10-5, https://doi.org/10.17190/AMF/1562392 (2024).
313. Network), N. N. E. O. Ameriflux base us-xle neon lenoir landing (leno), ver. 7-5, https://doi.org/10.17190/AMF/1773398 (2024).
314. Network), N. N. E. O. Ameriflux base us-xmb neon moab (moab), ver. 8-5, https://doi.org/10.17190/AMF/1671896 (2024).
315. Network), N. N. E. O. Ameriflux base us-xml neon mountain lake biological station (mlbs), ver. 8-5, https://doi.org/10.17190/AMF/1671897 (2024).
316. Network), N. N. E. O. Ameriflux base us-xng neon northern great plains research laboratory (nogp), ver. 9-5, https://doi.org/10.17190/AMF/1617732 (2024).
317. Network), N. N. E. O. Ameriflux base us-xnq neon onaqui-ault (onaq), ver. 9-5, https://doi.org/10.17190/AMF/1617733 (2024).
318. Network), N. N. E. O. Ameriflux base us-xnw neon niwot ridge mountain research station (niwo), ver. 8-5, https://doi.org/10.17190/AMF/1671898 (2024).
319. Network), N. N. E. O. Ameriflux base us-xrm neon rocky mountain national park, castnet (rmnp), ver. 9-5, https://doi.org/10.17190/AMF/1579723 (2024).
320. Network), N. N. E. O. Ameriflux base us-xrn neon oak ridge national lab (ornl), ver. 7-5, https://doi.org/10.17190/AMF/1773400 (2024).
321. Network), N. N. E. O. Ameriflux base us-xsb neon ordway-swisher biological station (osbs), ver. 8-5, https://doi.org/10.17190/AMF/1671899 (2024).
322. Network), N. N. E. O. Ameriflux base us-xsc neon smithsonian conservation biology institute (scbi), ver. 8-5, https://doi.org/10.17190/AMF/1671900 (2024).
323. Network), N. N. E. O. Ameriflux base us-xse neon smithsonian environmental research center (serc), ver. 9-5, https://doi.org/10.17190/AMF/1617734 (2024).
324. Network), N. N. E. O. Ameriflux base us-xsj neon san joaquin experimental range (sjer), ver. 8-5, https://doi.org/10.17190/AMF/1671901 (2024).
325. Network), N. N. E. O. Ameriflux base us-xsl neon north sterling, co (ster), ver. 9-5, https://doi.org/10.17190/AMF/1617735 (2024).
326. Network), N. N. E. O. Ameriflux base us-xsp neon soaproot saddle (soap), ver. 9-5, https://doi.org/10.17190/AMF/1617736 (2024).
327. Network), N. N. E. O. Ameriflux base us-xsr neon santa rita experimental range (srer), ver. 9-5, https://doi.org/10.17190/AMF/1579543 (2024).
328. Network), N. N. E. O. Ameriflux base us-xst neon steigerwaldt land services (stei), ver. 9-5, https://doi.org/10.17190/AMF/1617737 (2024).
329. Network), N. N. E. O. Ameriflux base us-xta neon talladega national forest (tall), ver. 8-5, https://doi.org/10.17190/AMF/1671902 (2024).
330. Network), N. N. E. O. Ameriflux base us-xte neon lower teakettle (teak), ver. 9-5, https://doi.org/10.17190/AMF/1617738 (2024).
331. Network), N. N. E. O. Ameriflux base us-xtr neon treehaven (tree), ver. 9-5, https://doi.org/10.17190/AMF/1634886 (2024).
332. Network), N. N. E. O. Ameriflux base us-xuk neon the university of kansas field station (ukfs), ver. 9-5, https://doi.org/10.17190/AMF/1617740 (2024).
333. Network), N. N. E. O. Ameriflux base us-xun neon university of notre dame environmental research center (unde), ver. 9-5, https://doi.org/10.17190/AMF/1617741 (2024).
334. Network), N. N. E. O. Ameriflux base us-xwd neon woodworth (wood), ver. 9-5, https://doi.org/10.17190/AMF/1579724 (2024).
335. Network), N. N. E. O. Ameriflux base us-xwr neon wind river experimental forest (wref), ver. 9-5, https://doi.org/10.17190/AMF/1617742 (2024).
336. Network), N. N. E. O. Ameriflux base us-xye neon yellowstone northern range (frog rock) (yell), ver. 9-5, https://doi.org/10.17190/AMF/1617743 (2024).

Acknowledgements

This work expanded upon exploratory analysis conducted by Sarah Marmolejos, a former undergraduate student in the Lowman Lab. This material is based upon work supported by the National Science Foundation under Award Number 2228047. The MODIS MCD12Q1 data were retrieved online from A$\rho\rho$EEARS and distributed by NASA Land Processes Distributed Active Archive Center (LP DAAC), http://appeears.earthdatacloud.nasa.gov/. Computations were performed using the Wake Forest University (WFU) High Performance Computing Facility, a centrally managed computational resource available to WFU researchers including faculty, staff, students, and collaborators[84]. Data from this material is stored by CUAHSI via HydroShare (http://www.hydroshare.org/resource/de74b0a457c74deca09f9a41afa03c8f) with support from the National Science Foundation (NSF) Cooperative Agreement No. EAR-1849458. We acknowledge the following AmeriFlux sites for their data records: CA-Ca3[85], CA-DSM[86], CA-ER1[87], CA-Gro[88], CA-Qfo[89], CA-TP1, CA-TP3[90], CA-TP2[91], CA-TP4[92], CA-TPD[93], MX-Aog[94], MX-Tes[95], US-Act[96], US-ADR[97], US-Akn[98], US-ALQ[99], US-AR1[100], US-AR2[101], US-ARb[102], US-ARc[103], US-ASH[104], US-ASL[105], US-ASM[106], US-Bar[107], US-Bi1[108], US-Bi2[109], US-Blo[110], US-Bo1[111], US-Bo2[112], US-BWa[113], US-BWb[114], US-CC1[115], US-CdM[116], US-Ced[117], US-CF1[118], US-CF2[119], US-CF3[120], US-CF4[121], US-Cop[122], US-CPk[123], US-CRK[124], US-CS1[125], US-CS2[126], US-CS3[127], US-CS4[128], US-CS5[129], US-CS6[130], US-CS8[131], US-Cst[132], US-Cwt[133], US-DFC[134], US-DFK[135], US-Dia[136], US-Dix[137], US-Dk1[138], US-Dk2[139], US-Dk3[140], US-Dmg[141], US-DPW[142], US-EA4[143], US-EA5[144], US-EA6[145], US-EDN[146], US-Elm[147], US-Esm[148], US-EvM[149], US-Fmf[150], US-Fuf[151], US-Fwf[152], US-GBT[153], US-GL1[154], US-GLE[155], US-Ha2[156], US-HB1, US-HB2, US-HB3[157], US-HB4[158], US-HBK[159], US-Ho1[160], US-Ho2[161], US-Ho3[162], US-Hsm[163], US-INa[164], US-INb[165], US-INc[166], US-INd[167], US-INe[168], US-INg[169], US-INi[170], US-INj[171], US-INn[172], US-INp[173], US-Jo2[174], US-KFS[175], US-KL1[176], US-KL2[177], US-KL3[178], US-KLS[179], US-KM1[180], US-KM2[181], US-KM3[182], US-KM4[183], US-Kon[184], US-KS1[185], US-KS2[186], US-KS3[187], US-KUT[188], US-LA1[189], US-LA2[190], US-Lin[191], US-LL1[192], US-LL2[193], US-LL3[194], US-Los[195], US-MC1[196], US-MC2[197], US-Me1[198], US-Me4[199], US-Me5[200], US-Men[201], US-MH1[202], US-MH2[203], US-Mj1, US-Mj2[204], US-MMS[205], US-MN1[206], US-MN3[207], US-Mo1[208], US-Mo2[209], US-Mo3[210], US-Mpj[211], US-MSR[212], US-MtB[213], US-MVF[214], US-MVW[215], US-Myb[216], US-NC1, US-NC2[217], US-NC3[218], US-NC4[219], US-NMj[220], US-NR1[221], US-NR3[222], US-NR4[223], US-ONA[224], US-OWC[225], US-PAS[226], US-PFa[227], US-PFf[228], US-PFo[229], US-PHM[230], US-Pnp[231], US-PSH[232], US-PSL[233], US-RC1[234], US-RC2[235], US-RC3[236], US-RC4[237], US-RC5[238], US-Ro1[239], US-Ro2[240], US-Ro3[241], US-Ro4[242], US-Ro5[243], US-Ro6[244], US-RRC[245], US-SdH[246], US-Seg[247], US-Ses[248], US-Slt[249], US-Snd[250], US-Sne[251], US-Snf[252], US-SP1[253], US-SP2[254], US-SP3[255], US-SP4[256], US-SRC[257], US-Srr[258], US-SRS[259], US-Sta[260], US-StJ[261], US-Syv[262], US-TaS[263], US-TEF[264], US-Ton[265], US-Tur[266], US-Tw1[267], US-Tw2[268], US-Tw3[269], US-Tw4[270],

US-Tw5[271], US-Twt[250], US-UiA[272], US-UiB[273], US-UiC[274], US-UiD[275], US-UM3[276], US-UMB[277], US-UTB[278], US-UTN[279], US-Var[280], US-Vcm[281], US-Vcp[282], US-Vcs[283], US-WCr[284], US-Wi0[285], US-Wi1[286], US-Wi2[287], US-Wi3[288], US-Wi4[289], US-Wi5[290], US-Wi6[291], US-Wi7[292], US-Wi8[293], US-Wi9[294], US-Wjs[295], US-Wrc[296], US-WT1[297], US-xAB[298], US-xAE[299], US-xBL[300], US-xBR[301], US-xCL[302], US-xCP[303], US-xDC[304], US-xDL[305], US-xDS[306], US-xGR[307], US-xHA[308], US-xJE[309], US-xJR[310], US-xKA[311], US-xKZ[312], US-xLE[313], US-xMB[314], US-xML[315], US-xNG[316], US-xnQ[317], US-xNW[318], US-xRM[319], US-xRN[320], US-xSB[321], US-xSC[322], US-xSE[323], US-xSJ[324], US-xSL[325], US-xSP[326], US-xSR[327], US-xST[328], US-xTA[329], US-xTE[330], US-xTR[331], US-xUk[332], US-xUN[333], US-xWD[334], US-xWR[335], US-xYE[336]. Funding for AmeriFlux data resources was provided by the U.S. Department of Energy's Office of Science.

Author contributions

L.L. conceptualized the idea for the research. P.T. provided guidance and input on the study design. N.C. and L.L. co-developed the methods for the study. N.C. implemented the methods, performed the data analysis, and wrote the original draft of the manuscript under the direction of L.L. All authors reviewed and edited the manuscript.

Competing interests

The authors declare no competing interests.

Additional information

Correspondence and requests for materials should be addressed to L.E.L.L.

Reprints and permissions information is available at www.nature.com/reprints.

Publisher's note Springer Nature remains neutral with regard to jurisdictional claims in published maps and institutional affiliations.